

# Multidecadal ozone trends in China and implications for human health and crop yields: A hybrid approach combining chemical transport model and machine learning

Jia Mao<sup>1</sup>, Amos Pui Kuen Tai<sup>1,2,3</sup>, David Ho Yin Yung<sup>1</sup>, Tiangang Yuan<sup>1</sup>, Kong Ting Chau<sup>1</sup>, and Zhaozhong Feng<sup>3,4</sup>

<sup>1</sup> Earth and Environmental Sciences Programme and Graduate Division of Earth and Atmospheric Sciences, Faculty of Science, The Chinese University of Hong Kong, Hong Kong SAR, China

<sup>2</sup> State Key Laboratory of Agrobiotechnology, and Institute of Environment, Energy and Sustainability, The Chinese University of Hong Kong, Hong Kong SAR, China

<sup>3</sup> Collaborative Innovation Center on Forecast and Evaluation of Meteorological Disasters (CIC-FEMD), Nanjing University of Information Science and Technology, Nanjing, Jiangsu, China

<sup>4</sup> Key Laboratory of Ecosystem Carbon Source and Sink, China Meteorological Administration (ECSS-CMA), Nanjing University of Information Science & Technology, Nanjing, Jiangsu, China

Correspondence to: Amos P. K. Tai ([amostai@cuhk.edu.hk](mailto:amostai@cuhk.edu.hk))

**Abstract.** Surface ozone (O<sub>3</sub>) is well known to pose significant threats to both human health and crop production worldwide. However, a multi-decadal assessment of O<sub>3</sub> impacts on public health and crop yields in China is lacking due to insufficient long-term continuous O<sub>3</sub> observations. In this study, we used a machine learning (ML) algorithm to correct the biases of O<sub>3</sub> concentrations simulated by the chemical transport model from 1981–2019 by integrating multi-source datasets. The ML-enabled bias correction offers improved performance in reproducing observed O<sub>3</sub> concentrations, and thus further improves our estimates of O<sub>3</sub> impacts on human health and crop yields. The warm-season increasing trend of O<sub>3</sub> in Beijing-Tianjin-Hebei and its surroundings (BTHs), Yangtze River Delta (YRD), Sichuan Basin (SCB) and Pearl River Delta (PRD) regions are 0.32 μg m<sup>-3</sup> yr<sup>-1</sup>, 0.63 μg m<sup>-3</sup> yr<sup>-1</sup>, 0.84 μg m<sup>-3</sup> yr<sup>-1</sup>, and 0.81 μg m<sup>-3</sup> yr<sup>-1</sup> from 1981 to 2019, respectively. In more recent years, O<sub>3</sub> concentrations experience more fluctuations in the four major regions. Our results show that only BTHs have a perceptible increasing trend of 0.81 μg m<sup>-3</sup> yr<sup>-1</sup> during 2013–2019. Using AOT40-China exposure-yield response relationships, the estimated relative yield losses (RYLs) for wheat, rice, soybean and maize are 17.6%, 13.8%, 11.3% and 7.3% in 1981, and increases to 24.2%, 17.5%, 16.3% and 9.8% in 2019, with an increasing rate of +0.03% yr<sup>-1</sup>, +0.04% yr<sup>-1</sup>, +0.27% yr<sup>-1</sup> and +0.13% yr<sup>-1</sup>, respectively. The estimated annual all-cause premature deaths induced by O<sub>3</sub> increase from ~55,900 in 1981 to ~162,000 in 2019 with an increasing trend of ~2,980 deaths yr<sup>-1</sup>. The annual premature deaths related to respiratory and cardiovascular disease are ~34,200 and ~40,300 in 1998, and ~26,500 and ~79,000 in 2019, having a rate of change of -546 and +1,770 deaths yr<sup>-1</sup> during 1998–2019, respectively. Our study, for the first time, used ML to provide a robust dataset of O<sub>3</sub> concentrations over the past four decades in China, enabling a long-term evaluation of O<sub>3</sub>-induced crop losses and health impacts. These findings are expected to fill the gap of the long-term O<sub>3</sub> trend and impact assessment in China.

## 1 Introduction

Surface ozone (O<sub>3</sub>), an important secondary air pollutant, is mainly generated through photochemical reaction of volatile organic compounds (VOCs), carbon monoxide (CO), and nitrogen oxides (NO<sub>x</sub>) in the presence of sunlight. As a strong oxidant, O<sub>3</sub> at the ground level is detrimental to human health and vegetation. More recently, due to the rapid

38 urbanization and industrialization, the summertime O<sub>3</sub> pollution has become an emerging concern in China. Li et al. (2020)  
39 reported that the mean summer 2013–2019 trend in maximum daily 8-h average surface O<sub>3</sub> (MDA8-O<sub>3</sub>) was +1.9 ppb yr<sup>-1</sup>  
40 in China, with high values widely observed in the North China Plain (NCP), Yangtze River Delta (YRD), and Pearl River  
41 Delta (PRD) regions. On the regional scale, the exposure of humans and vegetation to O<sub>3</sub> is greater in China than in other  
42 developed regions of the world (Lu et al., 2018). Several studies have suggested the important roles of climate and land  
43 cover changes on O<sub>3</sub> pollution in addition to anthropogenic emissions (Fu and Tai, 2015; Wang et al., 2020). It has been  
44 suggested that global warming and the changing land use may further increase surface O<sub>3</sub> by the late 21<sup>st</sup> century (Kawase  
45 et al., 2011; Wang et al., 2020), which can pose greater threats to human health and food security.

46 Meteorological factors can modulate the temporal and spatial patterns of O<sub>3</sub> via affecting the physical and chemical  
47 processes within the atmosphere (Liu et al., 2019; Mao et al., 2020; Yin and Ma, 2020). High temperature, low relative  
48 humidity and low planetary boundary height are conducive to the photochemical production and O<sub>3</sub> accumulation. Jacob  
49 and Winner (2009) summarized that the enhanced O<sub>3</sub> levels at higher temperatures are primarily driven by increased  
50 biogenic VOC emissions from vegetation and reduced lifetimes of peroxyacetyl nitrate (PAN) due to accelerated  
51 decomposition of PAN into NO<sub>x</sub>. Besides, the changes in wind speed and direction can affect O<sub>3</sub> concentrations through  
52 transport. Land cover and land use change affects O<sub>3</sub> air quality by perturbing surface fluxes, hydrometeorology, and  
53 concentrations of atmospheric chemical components (Tai et al., 2013; Fu and Tai, 2015; Liu et al., 2020; Ma et al., 2021).  
54 For instance, the terrestrial biosphere is a major source of isoprene, which plays a significant role in modulating O<sub>3</sub>  
55 concentrations. In the Intergovernmental Panel on Climate Change (IPCC) A1B scenario, Tai et al. (2013) found that  
56 widespread crop expansion could reduce isoprene emission by ~10 % globally compared with the present land use. Such  
57 a reduction could decrease O<sub>3</sub> by up to 4 ppb in the eastern US and increase O<sub>3</sub> by up to 6 ppb in South and Southeast Asia,  
58 whereby the difference in the sign of responses is primarily determined by the different O<sub>3</sub> production regimes.

59 The increasing health burden due to air pollution has become an important contributor to global disease burden. Some  
60 recent studies have demonstrated that short-term O<sub>3</sub> exposure negatively impacts human health, especially via respiratory,  
61 and cardiovascular mortality (Shang et al., 2013; Yin et al., 2017b; Feng et al., 2019; Zhang et al., 2022a). In 2015–2018,  
62 the estimated annual total premature mortality related to O<sub>3</sub> pollution in 334 Chinese cities was 0.27 million for 2015, 0.28  
63 million for 2016, 0.39 million for 2017, and 0.32 million for 2018 (Zhang et al., 2021). Maji and Namdeo (2021) reported  
64 that short-term all-cause, cardiovascular and respiratory premature mortalities attributed to the ambient 4<sup>th</sup> highest MDA8-  
65 O<sub>3</sub> exposure were 156,000, 73,500 and 28,600 in 2019, showing increases of 19.6%, 19.8% and 21.2%, respectively,  
66 compared to 2015. Zhang et al. (2022b) reported that each 10 µg m<sup>-3</sup> increase in the MDA8-O<sub>3</sub> can lead to a rise of 0.41 %  
67 (95 % CI: 0.35 %–0.48 %) in all-cause, 0.60 % (95 % CI: 0.51 %–0.68 %) in cardiovascular and 0.45 % (95 % CI: 0.28 %–  
68 0.62 %) in respiratory mortality.

69 The damage to plants induced by O<sub>3</sub> is mainly caused by the stomatal uptake of O<sub>3</sub> into the leaf interior instead of  
70 direct plant surface deposition (e.g., Clifton et al., 2020). In previous studies, a variety of concentration-based metrics have  
71 been widely used to assess the O<sub>3</sub> risks to crop yield and ecosystem functions. Initially, a 7-hour (09:00–15:59) mean metric  
72 (M7) was proposed, which was later extended to a 12-hour (08:00–19:59; referred to M12) to include late-day O<sub>3</sub>  
73 concentrations. Cumulative metrics have also been developed to evaluate the impacts of O<sub>3</sub> on crops. The accumulated O<sub>3</sub>  
74 over a threshold of 40 ppb (AOT40) is a widely used metric to evaluate the phytotoxic effects of O<sub>3</sub>. Compared to AOT40  
75 using a linear function, another metrics, W126, considers the nonlinear response of yield loss to O<sub>3</sub> exposure whereby  
76 higher O<sub>3</sub> concentrations will progressively induce more severe yield losses. However, many studies have suggested that  
77 the stomatal uptake of O<sub>3</sub> is more related to vegetation damage than O<sub>3</sub> exposure per se (Feng et al., 2012; Feng et al., 2018;  
78 Pleijel et al., 2022). In the recent two decades, the flux-based approach therefore has been developed and increasingly used  
79 to assess the relationships between the stomatal O<sub>3</sub> uptake and crop yields. Tai et al. (2021) compared the results of the  
80 estimated global crop yield losses using three concentration-based and two flux-based O<sub>3</sub> exposure metrics, and showed  
81 that the concentration-based metrics differ greatly among themselves, while the two flux-based metrics are generally close

82 to each other, which lie close to the middle of the range covered by all metrics.

83 At present, a comprehensive long-term assessment of O<sub>3</sub> impacts is hindered by a lack of continuous O<sub>3</sub> observations  
84 in China (Lu et al., 2018; Gong et al., 2021). From both health and food perspectives, reliable long-term estimates of O<sub>3</sub>  
85 are critically needed to better understand the O<sub>3</sub> damage over the past few decades since the beginning of rapid industrial  
86 transformation in the 1980s. In previous studies, various alternative approaches have been used to address the problem of  
87 insufficient observations. The multiple linear regression (MLR) model is often used for extrapolation to construct  
88 spatiotemporal distributions of air pollutants (Moustris et al., 2012; Abdullah et al., 2017). However, the linear statistical  
89 methods are generally limited by their incapability to capture the nonlinear relationships between air pollutants and  
90 precursors as well as meteorological fields. Chemical transport models (CTMs), based on mathematical representation of  
91 atmospheric physical and chemical processes, are also the common tool to simulate air pollutant concentrations  
92 spatiotemporally (Fusco and Logan, 2003; Liu and Wang, 2020a; Wang et al., 2022a). Taking the advantages of the CTM,  
93 Fu and Tai (2015) investigated the impacts of historical climate and land cover changes on tropospheric O<sub>3</sub> in East Asia  
94 between 1980 and 2010. However, the utility of CTMs is often limited by their high computational cost when conducting  
95 long-term simulations at high spatiotemporal resolutions. Large biases also exist due to uncertainties in historical emission  
96 inventories, parameterization of physical and chemical processes, and initial and/or boundary conditions, and these errors  
97 tend to increase at finer spatiotemporal scales.

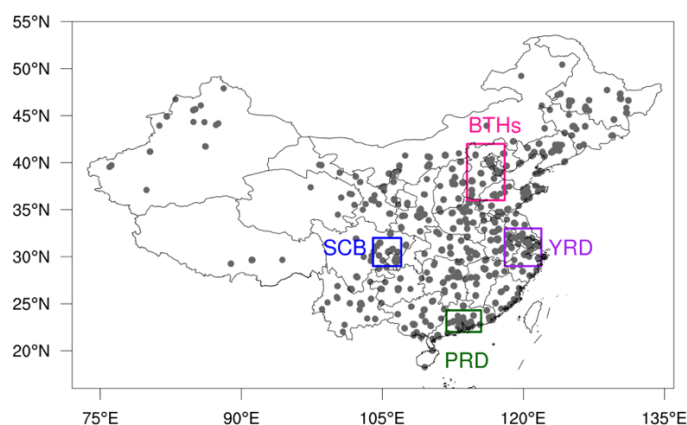
98 In recent years, machine learning (ML) methods have gained increasing popularity in air pollution studies (Liu et al.,  
99 2020; Ma et al., 2021). In the early stage of applying ML to atmospheric chemistry, ML methods were usually used as an  
100 independent method from CTMs (Hu et al., 2017; Zhan et al., 2017), for instance, to predict O<sub>3</sub> concentrations by mapping  
101 the nonlinear relationships between observed O<sub>3</sub> concentrations and their possible shaping factors. These applications are  
102 usually purely data-driven, whereby the ML algorithms do not involve any representation of the physical mechanisms  
103 behind the relevant processes. With powerful algorithms and user-friendly hyperparameter tuning processes, some well-  
104 trained ML models, driven by data from multiple sources including reanalysis and satellite data, have shown even higher  
105 predictive capacity than process-based models. The advantages of ML methods over CTMs include more flexible choices  
106 for input data and spatiotemporal resolution, and substantially lower computational costs (Bi et al., 2022). However, purely  
107 data-driven ML methods are known to suffer a lack of transparency and interpretability, which renders it more difficult to  
108 offer adequate scientific interpretation for the physical mechanisms behind. Thus, a hybrid approach combining ML  
109 algorithms and CTM-simulated results have been increasingly used to predict air pollutants and understand their trends in  
110 recent years. Integrating data from various sources, ML methods have been used as a tool to correct the biases in the lower-  
111 resolution simulated results from CTMs (Di et al., 2017; Ivatt and Evans, 2020; Ma et al., 2021). Based on process-based  
112 CTMs integrating decades of accumulated knowledge in Earth system science, while taking advantage of ML to address  
113 still-existing model errors, the hybrid approach has great potential in tackling air quality problems (Irrgang et al., 2021).

114 In this work, we incorporated the O<sub>3</sub> concentrations directly simulated by the Goddard Earth Observing System  
115 coupled with Chemistry (GEOS-Chem) model at a lower resolution into a bias-corrected, finer-resolution dataset by  
116 integrating them with O<sub>3</sub> observations from 2016 to 2018 (for validation purpose), high-resolution meteorological fields,  
117 land use data and other geographical information from multiple sources using a tree-based ML algorithm, LightGBM. The  
118 final high-resolution hourly O<sub>3</sub> dataset with a resolution of 0.25°×0.25° from 1981 to 2019 was further used to assess the  
119 impacts of O<sub>3</sub> on human health and crop yields over the past four decades. The simultaneous analysis of the combined  
120 impacts of O<sub>3</sub> on agriculture and human health can offer more comprehensive policy implications for the mitigation of O<sub>3</sub>-  
121 related impacts across China.

## 122 2 Data and methods

### 123 2.1 Air quality, meteorological, land and crop data

124 Hourly surface O<sub>3</sub> observations (μg m<sup>-3</sup>) from 2016 to 2018 were obtained from the China National Environment  
125 Monitoring Center Network (<http://106.37.208.233:20035/>) established by the Ministry of Ecology and Environment of  
126 China. The MDA8-O<sub>3</sub> of each site was calculated with at least 14 valid hourly values from 08:00 to 24:00 local time. A  
127 total of 1016 sites were selected after deleting the missing and abnormal data (**Fig. 1**).



128  
129 **Figure 1. Study domain and locations of the selected monitoring sites. The pink, blue, purple and green rectangles**  
130 **indicate the Beijing-Tianjin-Hebei and its surroundings (BTHs), Sichuan Basin (SCB), Yangtze River Delta (YRD),**  
131 **and Pearl River Delta (PRD) regions, respectively, for more detailed analysis.**

132 The surface meteorological fields used in this study include sea surface pressure, horizontal wind at 10 m, air  
133 temperature at 2 m, downward solar radiation, surface albedo, and total precipitation. The variables selected at 850 hPa  
134 and 100 hPa include relative humidity, horizontal and vertical velocity. These meteorological variables have been shown  
135 by many previous studies to correlate strongly with surface O<sub>3</sub> concentrations as discussed above. Hourly reanalysis data  
136 for meteorological variables were obtained from the fifth generation European Center for Medium-Range Weather  
137 Forecasts (ECMWF) reanalysis dataset (ERA5) with a spatial resolution of 0.25°×0.25° from 1981 to 2019  
138 (<https://cds.climate.copernicus.eu/>). This spatial resolution sets the highest limit of resolution for our hybrid O<sub>3</sub> product.

139 The national land use data with a spatial resolution of 1 km×1 km for 2013 were obtained from the Resource and  
140 Environment Science Data Center of the Chinese Academy of Sciences (RESDC) (<http://www.resdc.cn>). Six primary types  
141 of land use are considered: cultivated land, forestland, grassland, water bodies, construction land, and unused land.  
142 Nationwide elevation data were also provided by the RESDC (<https://www.resdc.cn/data.aspx?DATAID=123>), which is  
143 resampled based on the latest Shuttle Radar Topography Mission (SRTM) V4.1 data developed in 2000.

144 The spatial distribution of the harvested areas for four staple crops (wheat, rice, maize, soybean) for China was  
145 obtained from the Global Agro-Ecological Zones 2015 dataset (<https://doi.org/10.7910/DVN/KJFUO1>). Crop harvesting  
146 dates with a resolution of 0.5°×0.5° were provided by the Center for Sustainability and the Global Environment (Sacks et  
147 al., 2010). For crops having more than one growing season in a year, only the primary growing period was considered.

### 148 2.2 GEOS-Chem model

149 We used the GEOS-Chem global 3-D chemical transport model version 12.2.0 (<http://acmg.seas.harvard.edu/geos/>),  
150 driven by assimilated meteorological data from Modern Era Retrospective-analysis for Research and Applications, Version  
151 2 (MERRA2) (<https://gmao.gsfc.nasa.gov/reanalysis/MERRA-2/>) with a horizontal resolution of 2.0° latitude by 2.5°

152 longitude and reduced vertical resolution of 47 levels. GEOS-Chem incorporates meteorological conditions, emissions,  
153 chemical information, and surface conditions to simulate the formation, transport, mixing and deposition of ambient O<sub>3</sub>. It  
154 performs fully coupled simulations of O<sub>3</sub>-NO<sub>x</sub>-VOC-aerosol chemistry (Bey et al., 2001). Previous studies have  
155 demonstrated the ability of GEOS-Chem to reasonably reproduce the magnitudes and seasonal variations of surface O<sub>3</sub>  
156 East Asia (Wang et al., 2011; He et al., 2012). To provide long-term simulated O<sub>3</sub> fields for incorporation into the ML  
157 model (see below), we conducted GEOS-Chem simulations at a resolution of 2.0°×2.5°; higher resolutions of GEOS-Chem  
158 in nested grids are available but computationally prohibitive for multi-decadal simulations. The original unit of GEOS-  
159 Chem-simulated O<sub>3</sub> is ppb, which was converted to μg m<sup>-3</sup> assuming a constant temperature of 25°C and pressure of  
160 1013.25 hPa (1 μg m<sup>-3</sup> is approximately 0.5 ppb) when compared with observations (Yin et al., 2017b; Gong and Liao,  
161 2019).

162 Global anthropogenic emissions of CO, NO<sub>x</sub>, SO<sub>2</sub> and VOCs are from Community Emissions Data System (CEDS),  
163 which has coverage over the simulation years of 1950–2014 (Hoesly et al., 2018). Biomass burning emissions are from the  
164 GFED-4 inventory (van der Werf et al., 2017). Biogenic VOC emissions are computed by the Model of Emissions of Gases  
165 and Aerosols from Nature (MEGAN) v2.1 (Guenther et al., 2012), which is embedded in GEOS-Chem. Emissions of  
166 biogenic VOC species in each grid cell, including isoprene, monoterpenes, methyl butenol, sesquiterpenes, acetone and  
167 various alkenes, are simulated as a function of canopy-scale emission factors modulated by environmental activity factors  
168 to account for changing temperature, light, leaf age, leaf area index (LAI), soil moisture and CO<sub>2</sub> concentrations  
169 (Sindelarova et al., 2014).

170 Dry deposition follows the resistance-in-series scheme of Wesely (1989), which depends on species properties, land  
171 cover types and meteorological conditions, and uses the Olson land cover classes with 76 land types reclassified into 11  
172 land types. Although transpiration is a potential mechanism via which the land cover affects ozone, we do not address it in  
173 this study because water vapor concentration in GEOS-Chem is prescribed from assimilated relative humidity (i.e., not  
174 computed online from evapotranspiration).

### 175 **2.3 LightGBM machine-learning model**

176 The primary purpose of utilizing ML here was to minimize the biases of model output as compared with observations,  
177 whereby the biases could arise from incomplete model physics, input and parameter errors, numerical errors, coding errors,  
178 as well as representation errors (i.e., mismatch in spatial scales between model grid cells and site observations), so that the  
179 output of the hybrid model could have the closest values to the observations and enable more accurate impact evaluation.  
180 In this study, we used the LightGBM ML algorithm to integrate GEOS-Chem-simulated O<sub>3</sub> at a lower resolution with  
181 higher-resolution multi-source data to produce higher-resolution hourly O<sub>3</sub> and MDA8-O<sub>3</sub> fields.

182 LightGBM is a ML algorithm based on the gradient boosting decision tree (Chen and Guestrin, 2016), which has a  
183 high training efficiency and lower memory footprint, and thus is suitable for processing massive high-dimensional data  
184 (Zhang et al., 2019). The general steps to build a ML model can be summarized as follows: (1) choose an algorithm  
185 appropriate for the problem (e.g., regression or classification); (2) clean the data and split them into training and test data;  
186 (3) train and tune the model with training data to well capture prediction patterns; (4) evaluate model performance on test  
187 data; and (5) return to step (3) and (4) until an optimal predictive ability is reached. The training and evaluation processes  
188 are both performed at the site level in accordance with the observations, whereby the predictor variables and model  
189 responses were first sampled at the same locations using the bilinear interpolation approach (Accadia et al., 2003). This  
190 approach of handling spatial scale mismatch between model grid cells and site observations has been commonly used in  
191 previous studies (e.g., Li et al., 2021). When predicting the gridded O<sub>3</sub> concentrations with the trained model, predictor  
192 variables at different spatial resolutions were all regridded to the same resolution of 0.25°×0.25° consistent with the ERA5  
193 meteorological fields. By taking the advantage of these higher-resolution datasets, the hybrid approach can not only correct

194 the biases of the GEOS-Chem-simulated O<sub>3</sub>, but also refine them into a finer resolution. To evaluate if the hybrid approach  
195 truly benefits from using a higher-resolution meteorological fields, we also repeated the whole training exercise with the  
196 input meteorology of GEOS-Chem (MERRA2 at 2.0°×2.5°) instead of ERA5.

197 During the model training process, the model was evaluated with 10-fold cross-validation to ensure the robustness  
198 and reliability of the model, whereby the training data were randomly partitioned into 10 subsets of approximately the same  
199 size, with 90% of data used to train individual models and the ensemble model, and the remaining 10% of data used to  
200 examine model performance (Xiao et al., 2018). This process was repeated 10 times so that each data record was left for  
201 testing once. The tuning of the hyperparameters was optimized using grid search optimization to improve detection  
202 performance and diagnostic accuracy (Wang et al., 2019). Statistical indicators, including the coefficient of determination  
203 ( $R^2$ ) and root-mean-square error (RMSE), were used in subsequent assessment of model performance for GEOS-Chem  
204 alone and for the hybrid approach.

205 Our analysis revealed that training the model with one year or more of data results in only marginal reductions in  
206 RMSE and enhancements in  $R^2$  (Fig. S1); thus a timescale of two years appears to strike a good balance between  
207 computational burden and model accuracy. These results align with the findings of Ivatt and Evans (2020), who suggested  
208 that much of the variability in the power spectrum of surface O<sub>3</sub> can be captured by timescales of a year or less. Therefore,  
209 here we utilized observations from the period 2016-2017 as the training data, which offered a more economical computing  
210 cost and improved training time efficiency, and observations in 2018 as the independent test data to evaluate model  
211 performance.

## 212 2.4 Ozone exposure metric and exposure–yield response functions

213 Among O<sub>3</sub> exposure indices, AOT40 has been used widely during the last two decades as it has been found to have a  
214 strong relationship with relative yield of many crop species (Mills et al., 2007), and thus was used to quantify the impacts  
215 of surface O<sub>3</sub> on crop yields in this study. The flux-based metrics, which require long-term simulations using a process-  
216 based stomatal uptake model, were beyond the scope of this study. The AOT40 (ppm-h) is defined as follows:

$$217 \text{AOT40} = \sum_{i=1}^n ([\text{O}_3]_i - 0.04) \quad (1)$$

218 where the  $[\text{O}_3]_i$  is the hourly mean O<sub>3</sub> concentration (ppm) during the 12 hours of local daytime (08:00–19:59);  $n$  is the  
219 number of hours in the growing season defined as the 90 days prior to the start of the harvesting period according to the  
220 crop calendar.

221 The exposure–yield response functions based on extensive field experimental studies have been established to relate  
222 a quantifiable O<sub>3</sub>-exposure metrics to crop yields. It has been suggested that responses of crop yields were found greater  
223 in Asian experiments than the American and European counterparts, indicating possibly higher O<sub>3</sub> sensitivity of Asian crop  
224 varieties (Emberson et al., 2009; Feng et al., 2022). To better understand O<sub>3</sub>-induced risks to crops in China, the AOT40  
225 exposure-yield functions developed based on field experiments in China are used in this study, which are named as AOT40-  
226 China. The exposure–yield response functions for soybean is from Zhang et al. (2017), and for other three crops are from  
227 Feng et al. (2022). The statistical exposure-yield relationships used in this study are summarized in **Table S1**.

## 228 2.5 Analysis of health impacts

229 All-cause mortality, cardiovascular disease mortality and respiratory disease mortality are selected as the health  
230 outcomes of our study due to the high correlation between these endpoints and short-term O<sub>3</sub> exposure in previous studies.  
231 A log-linear exposure-response function is widely adopted and recommended by the World Health Organization (WHO)  
232 for health impact assessment in areas with severe air pollution. In particular, the log-linear model is the most widely applied

233 exposure-response model at present in China (Lelieveld et al., 2015; Yin et al., 2017a; Zhang et al., 2022b). The premature  
234 mortality is calculated following:

$$235 \quad \Delta M = \delta c * \left[ \frac{(RR - 1)}{RR} \right] * P \quad (2)$$

236 where  $\Delta M$  is the excess mortality attributable to O<sub>3</sub> exposure;  $\delta c$  is the baseline mortality rate for a particular health endpoint  
237 (Yin et al., 2017b; Madaniyazi et al., 2016);  $P$  is the exposed population; and RR is the relative risk defined as:

$$238 \quad RR = \exp( (X - X_0) * \beta ) \quad (3)$$

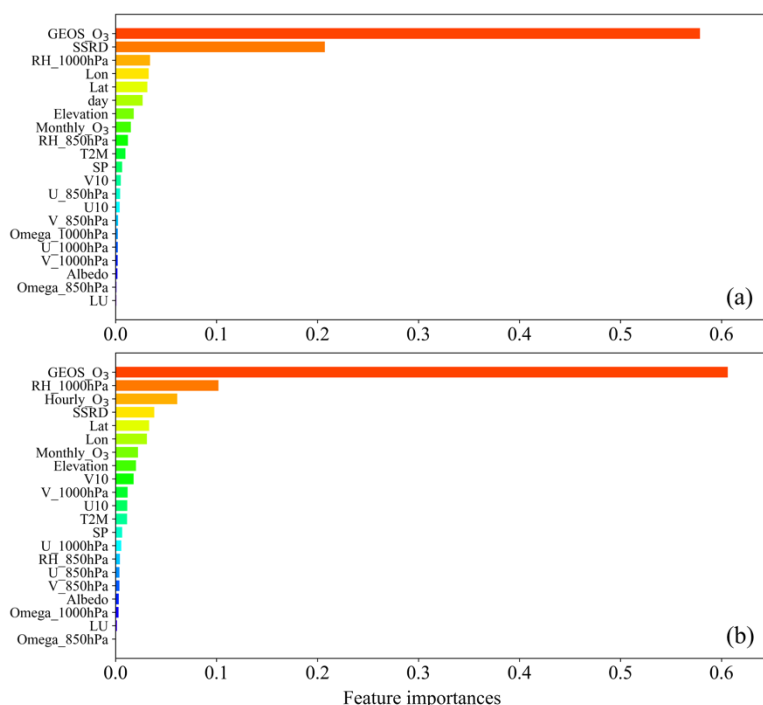
239 where  $\beta$  is the exposure-response coefficient derived from epidemiological cohort studies (Shang et al., 2013);  $X$  represents  
240 the model-calculated O<sub>3</sub> concentration; the value of  $X_0$  is the threshold concentration below which no additional risk is  
241 assumed. Consistent with previous studies (Lelieveld et al., 2015; Liu et al., 2018), we used  $X_0 = 75.2 \mu\text{g m}^{-3}$ .

242 In this study, the mean MDA8-O<sub>3</sub> concentrations in warm season (May-September) were used to estimate the disease-  
243 specific health impacts of short-term exposure to O<sub>3</sub>. The province-level population and national baseline mortality rate for  
244 particular diseases were provided by the National Bureau of Statistics (<http://www.stats.gov.cn/>). The spatial differences of  
245 baseline mortality in China were not considered without provincial-level data, which means that we assume the baseline  
246 mortality is evenly distributed across China (Dedoussi et al., 2020). The exposure-response coefficients were obtained from  
247 existing epidemiological studies in China (**Table S2**). If the corresponding coefficient of a province could not be found in  
248 published epidemiological studies, the datum closest to that province would be selected as a substitute. If there were no  
249 neighboring provinces, the results of national meta-analysis would be used (Zhang et al., 2021).

## 250 **3 Results**

### 251 **3.1 Model development and validation**

252 The finally selected features and their importance estimated by the LightGBM algorithm based on 10-fold cross  
253 validation are shown in **Fig. 2**. GEOS-Chem-simulated O<sub>3</sub> is the top predictor for predicting surface O<sub>3</sub> concentrations,  
254 accounting for 61% and 58% of all relative importance in the ML algorithm predicting hourly O<sub>3</sub> and daily MD8A-O<sub>3</sub>,  
255 respectively. The result indicates that process-based GEOS-Chem simulations have high utility for O<sub>3</sub> predictions under  
256 the hybrid approach (Ma et al., 2021). The meteorological variables with high contribution to both the daily and hourly  
257 models are downward surface solar radiation (SSRD), relative humidity at 1000 hpa (RH\_1000hpa) and 10-m horizontal  
258 wind (U10 and V10). Other special features, including location (latitude and longitude), elevation and diurnal and monthly  
259 pattern of O<sub>3</sub>, also contribute to ambient O<sub>3</sub> estimations. The spatial distributions of bias-corrected O<sub>3</sub> are consistent with  
260 observations for both training and test datasets (**Fig. S2**), indicating that there is no obvious overfitting, i.e., the model is  
261 able to generalize from the training set to the test set. The good generalization ability of the model gives us confidence in  
262 its ability to make accurate predictions based on new data. In general, the hybrid approach can yield good O<sub>3</sub> estimates in  
263 the data-intensive regions, including eastern and central China that are the hotspot areas of O<sub>3</sub> pollution.



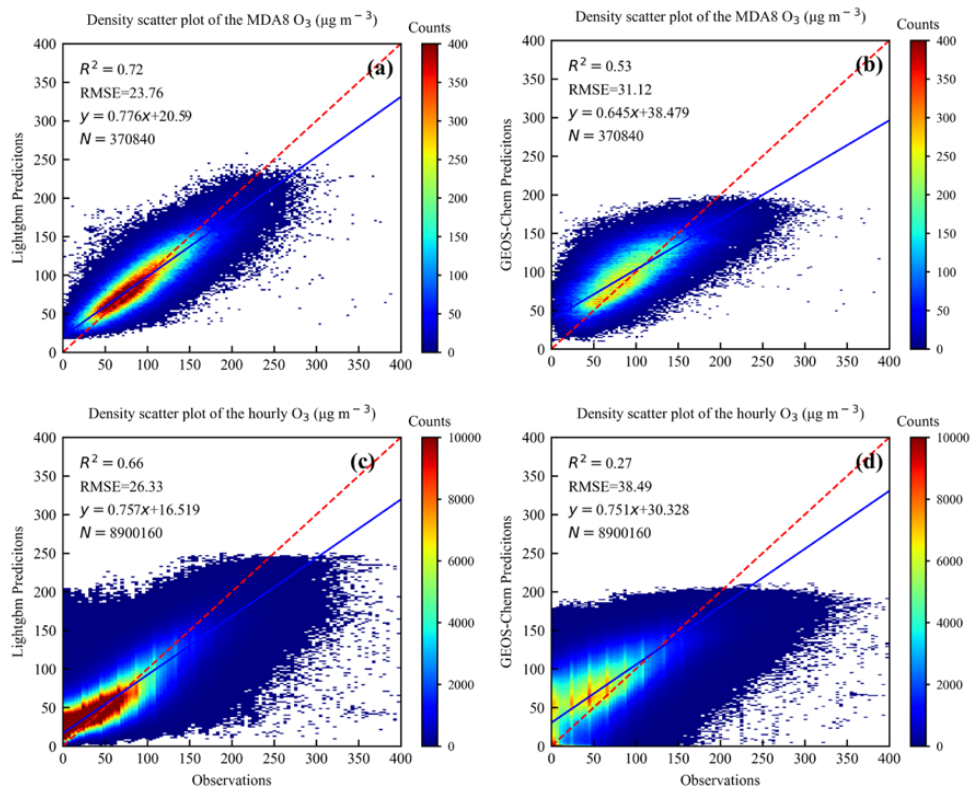
264  
 265 **Figure 2. The feature importance plot for (a) MDA8-O<sub>3</sub> and (b) hourly O<sub>3</sub>, respectively. The full list of candidate**  
 266 **variables with their symbols, units, descriptions, and data sources are shown in Table S3.**

267 **Fig. 3** shows the density scatter plots between O<sub>3</sub> measurements and GEOS-Chem simulations, as well as the hybrid-  
 268 approach predictions for 2018. The  $R^2$  value of the hybrid approach and GEOS-Chem model are 0.66 and 0.27 at hourly  
 269 level, and 0.72 and 0.53 at MDA8-O<sub>3</sub> level, respectively. Bias-corrected O<sub>3</sub> concentrations have lower RMSE in  
 270 comparison with GEOS-Chem simulated O<sub>3</sub> concentrations, reduced from 31.1 to 23.8  $\mu\text{g m}^{-3}$  for MDA8-O<sub>3</sub> predictions,  
 271 and from 38.5 to 26.3  $\mu\text{g m}^{-3}$  for hourly predictions. The MDA8-O<sub>3</sub> model performance is better than that of the hourly  
 272 model, indicating reduced errors upon temporal averaging. To test if using the higher-resolution meteorological data offers  
 273 better prediction accuracy compared with the original input meteorology of GEOS-Chem, the MERRA2 dataset driving  
 274 GEOS-Chem was also used to train the model. We found that the higher-resolution ERA5 dataset performed better in  
 275 reproducing observed O<sub>3</sub> concentrations with moderately smaller RMSE and larger  $R^2$  (**Fig. S3**), demonstrating the level  
 276 to which a higher-resolution meteorological dataset, despite not being strictly consistent with the input meteorology for the  
 277 CTM, can help enhance the performance of the hybrid approach and help resolve finer spatial details within the original  
 278 CTM grid cells. In summary, the result suggests that the CTM-simulated results can be substantially improved by applying  
 279 ML with multi-source datasets, and the bias-corrected data can improve our understanding of long-term O<sub>3</sub> trends and its  
 280 further implications on crop and human health over China, as discussed in the following sections.

281 In comparison with previous studies, Liu et al. (2020) used XGBoost to predict O<sub>3</sub> in major urban areas of China at a  
 282 resolution of  $0.1^\circ \times 0.1^\circ$ , and the  $R^2$  value and RMSE for MDA8-O<sub>3</sub> were 0.74 and 23.8  $\mu\text{g m}^{-3}$ , respectively. Their result  
 283 indicates that higher-resolution predictions may help enhance model accuracy, but represent a trade-off between model  
 284 accuracy and time efficiency depending on the purpose. Instead of directly predicting O<sub>3</sub> concentrations, Ivatt and Evans  
 285 (2020) predicted biases in GEOS-Chem-simulated O<sub>3</sub> concentrations and then corrected them with XGBoost. They also  
 286 suggested that the corrected model performs considerably better than the uncorrected model, with RMSE reduced from  
 287 32.4 to 15.0  $\mu\text{g m}^{-3}$  and Pearson's  $R$  raised from 0.48 to 0.84. Their greater improvement with larger reduced RMSE than  
 288 our result is mainly because they selected fewer sites for training, with all the urban and mountain sites (observations made  
 289 at a pressure < 850 hPa) removed. The removal of these sites can improve the overall apparent performance of the model  
 290 because O<sub>3</sub> formation could have different characteristics in these areas. In general, ML methods have been proven to be a



291 promising tool to improve air pollutant forecasts when a process-level understanding is still incomplete.



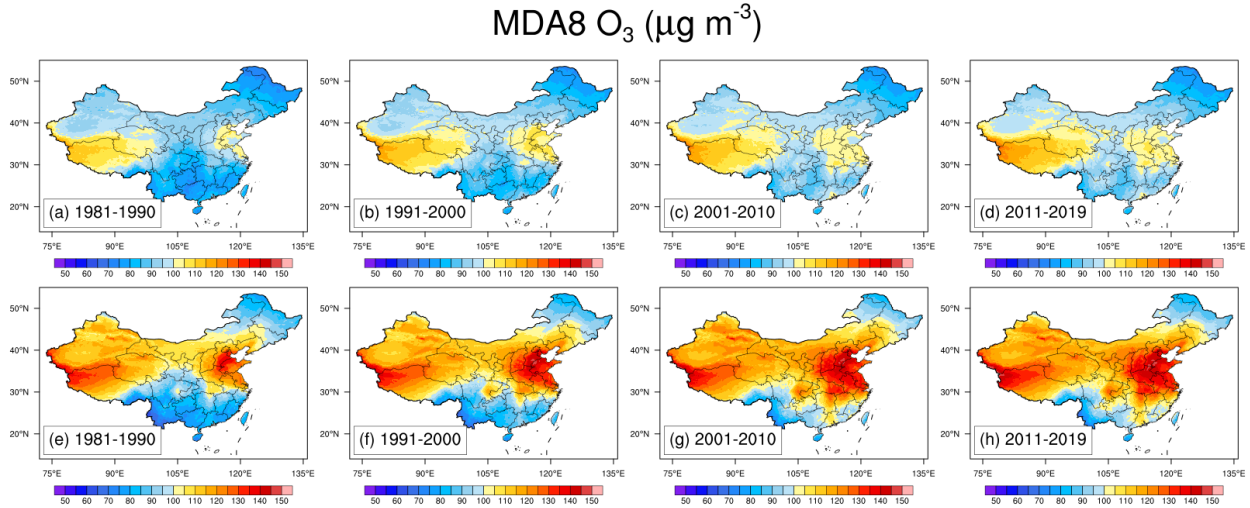
292

293 **Figure 3. Density scatter plots and linear regression statistics of O<sub>3</sub> predictions vs. observation for 2018: (a) bias-**  
294 **corrected MDA8-O<sub>3</sub> vs. observations; (b) GEOS-Chem MDA8-O<sub>3</sub> vs. observations; (c) bias-corrected hourly O<sub>3</sub> vs.**  
295 **observations; and (d) GEOS-Chem hourly O<sub>3</sub> vs. observations. The model results are sampled at the same locations.**  
296 **The dashed red line indicates the 1:1 line, and the solid blue line indicates the line of best fit using orthogonal**  
297 **regression. The  $R^2$  is the coefficient of determination, RMSE is the root-mean-square error, and  $N$  is the number of**  
298 **data points. The X and Y axis represents the O<sub>3</sub> observations and predictions, respectively.**

299

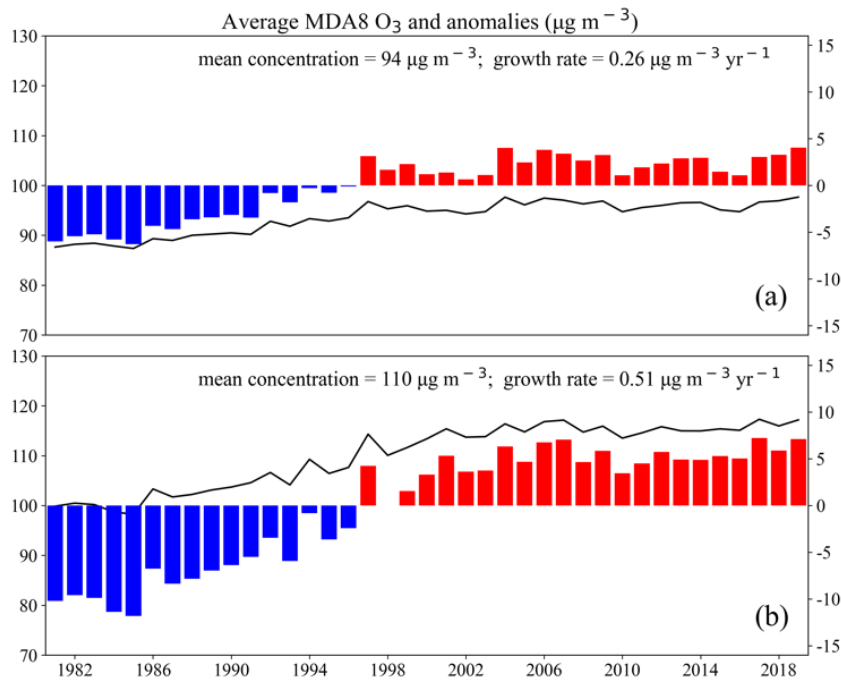
### 300 3.2 Spatiotemporal distribution and trends of O<sub>3</sub> predictions

301 **Fig. 4** demonstrates the spatial patterns of averaged annual and warm-season (May-September) MDA8-O<sub>3</sub> from 1981  
302 to 2019. When compared to the high concentrations in the warm season, MDA8-O<sub>3</sub> concentrations are relatively lower at  
303 annual level. The annual and warm-season MDA8-O<sub>3</sub> concentrations have similar spatial distribution, and both present an  
304 increasing trend over the past decades, with more substantial increase observed between 1981 and 2010. The O<sub>3</sub> levels in  
305 southern China are lower than those in northern China, but they are still relatively high in the PRD region, which is  
306 consistent to findings in previous studies (e.g. Liu and Wang, 2020a). During the first decade of 1981–1990, high O<sub>3</sub>  
307 concentration areas are mainly concentrated in the BTHs and northern Shandong. In the next two decades, O<sub>3</sub> pollution  
308 extensively expands to most of East and North China, spreading northward to Jilin and Liaoning, westward to Shanxi and  
309 Ningxia, and southward to northern Hunan, Shanxi and Zhejiang. Moreover, the SCB and PRD regions also experience  
310 aggravated O<sub>3</sub> pollution during this period. In the last decade of the study period, O<sub>3</sub> concentrations remain at high levels  
311 in BTHs and SCB without obvious changes. To understand the detailed changes and trends of O<sub>3</sub>, next we analyze the  
312 interannual variability.



313  
 314 **Figure 4. Spatial distribution of the annual mean MDA8-O<sub>3</sub> concentrations (μg m<sup>-3</sup>) during: (a) 1981–1990; (b)**  
 315 **1991–2000; (c) 2001–2010; and (d) 2011–2019. Spatial distribution of the warm-season (May–September) mean**  
 316 **MDA8-O<sub>3</sub> concentrations of (e)1981–1990, (f) 1991–2000, (g) 2001–2010; and (h) 2011–2019.**

317 **Fig. 5** shows that the annual averaged MDA8-O<sub>3</sub> concentrations increase from 87 μg m<sup>-3</sup> in 1981 to 98 μg m<sup>-3</sup> in  
 318 2019, with a growth rate of +0.26 μg m<sup>-3</sup> yr<sup>-1</sup>, while the warm-season averaged MDA8-O<sub>3</sub> concentrations increase from  
 319 100 μg m<sup>-3</sup> in 1981 to 117 μg m<sup>-3</sup> in 2019, having a growth rate of +0.51 μg m<sup>-3</sup> yr<sup>-1</sup>. Moreover, the average annual and  
 320 warm-season O<sub>3</sub> concentrations have a more obvious upward trend before 2000s, with a growth rate of 0.38 μg m<sup>-3</sup> yr<sup>-1</sup>  
 321 and 0.71 μg m<sup>-3</sup> yr<sup>-1</sup>, compared to that after 2000s, when O<sub>3</sub> concentrations appear to fluctuate within a certain range.  
 322 GEOS-Chem-simulated O<sub>3</sub> has a similar trend as the bias-corrected O<sub>3</sub>, but it generally overestimates O<sub>3</sub> concentrations on  
 323 national scale (**Fig. S4**). The annual and warm-season averaged MDA8-O<sub>3</sub> concentrations in BTHs, YRD, SCB and PRD  
 324 regions are shown in **Fig. S5–S6**. The warm-season increasing trend for BTHs, YRD, SCB and PRD regions are 0.32 μg  
 325 m<sup>-3</sup> yr<sup>-1</sup>, 0.63 μg m<sup>-3</sup> yr<sup>-1</sup>, 0.84 μg m<sup>-3</sup> yr<sup>-1</sup>, and 0.81 μg m<sup>-3</sup> yr<sup>-1</sup> from the year 1981 to 2019.



326  
 327 **Figure 5. The bias-corrected MDA8-O<sub>3</sub> predictions (black line; left y axis) and corresponding anomalies (colored**

328 **bar; right y axis) from 1981 to 2019: (a) annual mean; and (b) warm-season mean (May–September). The trends**  
 329 **(growth rates) are obtained by ordinary linear regression on mean values of MDA8-O<sub>3</sub>. The anomalies are defined**  
 330 **as annual mean minus the multidecadal average over 1981–2019.**

331 In recent years, the worsening O<sub>3</sub> pollution has fueled numerous studies on ground-level O<sub>3</sub> spatial distribution and  
 332 changes in China, which were conducted on local, regional and national scale using different O<sub>3</sub> fields from observations,  
 333 CTMs and ML estimates. In this study, we mainly focus on the regional and national O<sub>3</sub> characteristics, and the reported  
 334 O<sub>3</sub> trends in recent studies are listed in **Table 1**. By comparing the results of existing works, we find that source-varied O<sub>3</sub>  
 335 fields can induce great uncertainty of the O<sub>3</sub> trends. Moreover, the O<sub>3</sub> trends are found to be very sensitive to the study  
 336 period even with the same O<sub>3</sub> fields (Wei et al., 2022), which indicates large interannual variability, mostly reflecting the  
 337 changing anthropogenic emissions and meteorology (Lu et al., 2019; Li et al., 2020). In contrast to the perceptible O<sub>3</sub> trends,  
 338 Liu et al. (2020) suggested that O<sub>3</sub> pollution in most parts of China has only modest changes between 2005 and 2017, and  
 339 their trends were not spatially continuous. Wang et al. (2022b) also reported that O<sub>3</sub> has small positive increase rates for  
 340 2013–2021 in many cities, and the O<sub>3</sub> increase rates greatly differ from site to site even within the same region.

341 In comparison, our results indicate no obvious increasing trends of national MDA8-O<sub>3</sub> within the same study period.  
 342 On a regional scale, only BTHs have a perceptible increasing trend in more recent years, while no such trends are found  
 343 over the YRD, SCB and PRD regions during the same period. The summertime MDA8-O<sub>3</sub> in BTHs has a change rate of  
 344 +0.81 μg m<sup>-3</sup> yr<sup>-1</sup>, which is much lower than the results using O<sub>3</sub> observations (Li et al., 2020). One possible reason is that  
 345 most observational sites are in urban regions, which usually suffer more serious O<sub>3</sub> pollution, while the O<sub>3</sub> concentrations  
 346 from model simulations and ML methods are calculated on the scale of a grid cell with lower domain-averaged values.  
 347 Moreover, gridded data at a relatively coarse resolution may fail to capture larger site differences, leading to the larger  
 348 discrepancy of between O<sub>3</sub> observations and gridded O<sub>3</sub> estimates.

349 **Table 1 Summary of reported regional and national MDA8-O<sub>3</sub> trends (μg m<sup>-3</sup> yr<sup>-1</sup>).**

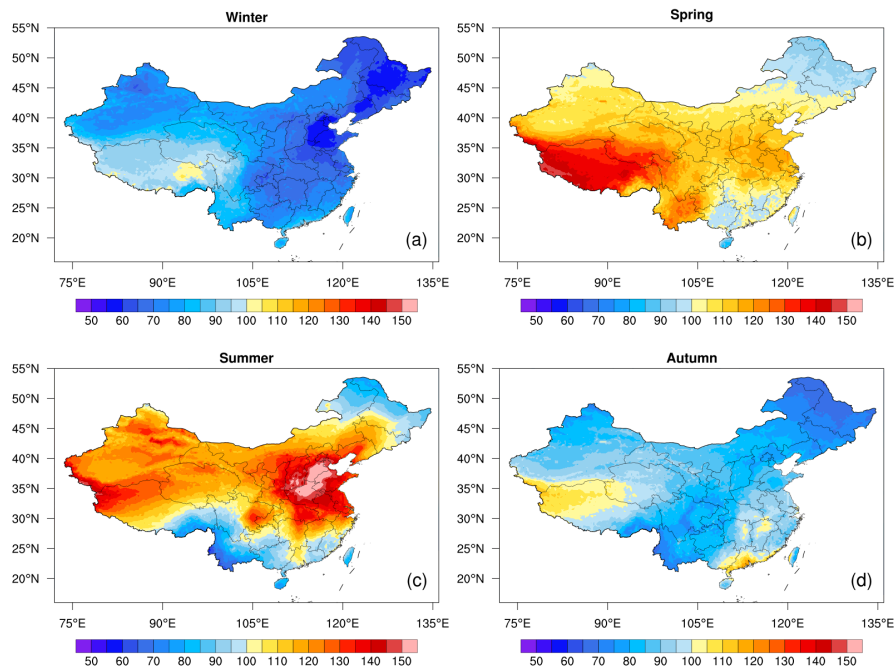
Region	Period	Increase rate	Data source/Method	References
Nation	2013–2017 (annual)	0.35	ML (XGBoost)	(Liu et al., 2020)
	2013–2017 (annual)	0.92	WRF-CMAQ	(Liu and Wang, 2020b)
	2013–2017 (annual)	1.33	ML (ERT)	(Wei et al., 2022)
	2015–2019 (annual)	4.40	ML (ERT)	(Wei et al., 2022)
	2015–2019 (annual)	1.90	Observations	(Maji and Namdeo, 2021)
	2013–2019 (summer)	3.80	Observations	(Li et al., 2020)
	1981–2019 (annual)	0.26	ML (LightGBM)	This study
	1981–2000 (annual)	0.38	ML (LightGBM)	This study
	1981–2019 (warm-season)	0.51	ML (LightGBM)	This study
BTH	1981–2000 (warm-season)	0.71	ML (LightGBM)	This study
	2010–2017 (annual)	0.60	ML (Random Forest)	(Ma et al., 2021)
	2013–2017 (annual)	1.33	ML (XGBoost)	(Liu et al., 2020)
	2013–2017 (annual)	4.78	ML (ERT)	(Wei et al., 2022)
	2012–2017 (summer)	1.16	GEOS-Chem	(Dang et al., 2021)
	2013–2019 (summer)	6.60	Observations	(Li et al., 2020)
	1981–2019 (summer)	0.46	ML (LightGBM)	This study
YRD	2013–2019 (summer)	0.81	ML (LightGBM)	This study
	2013–2017 (annual)	2.94	ML (ERT)	(Wei et al., 2022)
	2015–2019 (annual)	5.60	ML (ERT)	(Wei et al., 2022)
	2012–2017 (summer)	3.48	GEOS-Chem	(Dang et al., 2021)
	2013–2019 (summer)	3.20	Observations	(Li et al., 2020)
	1981–2019 (annual)	0.24	ML (LightGBM)	This study
SCB	1981–2019 (summer)	0.73	ML (LightGBM)	This study
	2013–2017 (annual)	2.37	ML (ERT)	(Wei et al., 2022)

	2013–2019 (summer)	1.40	Observations	(Li et al., 2020)
	1981–2019 (annual)	0.48	ML (LightGBM)	This study
	1981–2019 (summer)	0.98	ML (LightGBM)	This study
PRD	2007–2017 (annual)	1.20	Observations	(Yang et al., 2019)
	2013–2017 (annual)	−0.72	ML (ERT)	(Wei et al., 2022)
	2015–2019 (annual)	4.38	ML (ERT)	(Wei et al., 2022)
	2013–2019 (summer)	2.20	Observations	(Li et al., 2020)
	1981–2019 (annual)	0.56	ML (LightGBM)	This study
	1981–2019 (fall)	0.69	ML (LightGBM)	This study

350

### 351 3.3 Seasonal characteristics of O<sub>3</sub> predictions

352 Differences in averaged annual and warm-season O<sub>3</sub> concentrations indicate that O<sub>3</sub> has distinctive seasonal  
353 characteristics. **Fig. 6** shows the seasonal variations in O<sub>3</sub> concentrations from 2011–2019, and results for other past three  
354 decades are shown in **Fig. S7-S9**. In winter, pollution is mainly concentrated in the coastal areas of southern China. In  
355 spring, O<sub>3</sub> pollution primarily occurs in eastern China and the southern part of Yunnan Province. O<sub>3</sub> pollution continues to  
356 aggravate over eastern China in summer, particularly in BTHs, and further extends to SCB. The air quality in eastern and  
357 central China is greatly improved in fall, while southern China experiences the most pollution in this period. In general,  
358 the peak and trough values of O<sub>3</sub> concentrations appear in summer and winter, respectively. However, O<sub>3</sub> concentrations  
359 are found to be minimum in summer and maximum in fall over PRD, which is largely determined by the summer monsoon  
360 (Zhou et al., 2013; Wang et al., 2018a). **Fig. S10** shows the seasonal averaged MDA8-O<sub>3</sub> concentrations in different regions  
361 from 1981 to 2019. In winter, O<sub>3</sub> concentrations do not have much change across the four regions over the past decades,  
362 staying mostly between 70–80 µg m<sup>-3</sup>. Moreover, wintertime O<sub>3</sub> concentrations after the 2000s are generally lower than  
363 that before the 2000s in BTHs, YRD and SCB. In contrast, summertime O<sub>3</sub> concentrations have a dramatic increase over  
364 the four regions. In spring and fall, O<sub>3</sub> concentrations have an increasing trend in PRD, while it mostly fluctuates within a  
365 certain range in the other three regions. The results show that O<sub>3</sub> in non-winter seasons has a more pronounced increase  
366 during 1981–2019 albeit with regional differences. The regional characteristics of O<sub>3</sub> and its influencing factors will be  
367 further discussed in Section 3.4. The BTH, SCB, YRD, and PRD regions have been identified as hotspots of O<sub>3</sub> pollution  
368 in China. These regions are characterized by high population density (Wang et al., 2018b) and are also major agricultural  
369 areas (Monfreda et al., 2008), which may face greater burdens of crop yield and human health losses with high O<sub>3</sub>  
370 concentrations. Therefore, here we provide more detailed analysis and investigation of these regions.



371

372 **Figure 6. Spatial distribution of the bias-corrected MDA8-O<sub>3</sub> predictions ( $\mu\text{g m}^{-3}$ ) from 2011–2019: (a) winter; (b)**  
 373 **spring; (c) summer; and (d) fall.**

374

### 3.4 Regional characteristics of O<sub>3</sub> predictions

375

376

377

378

379

380

381

382

383

384

385

386

387

388

389

390

391

392

393

394

395

396

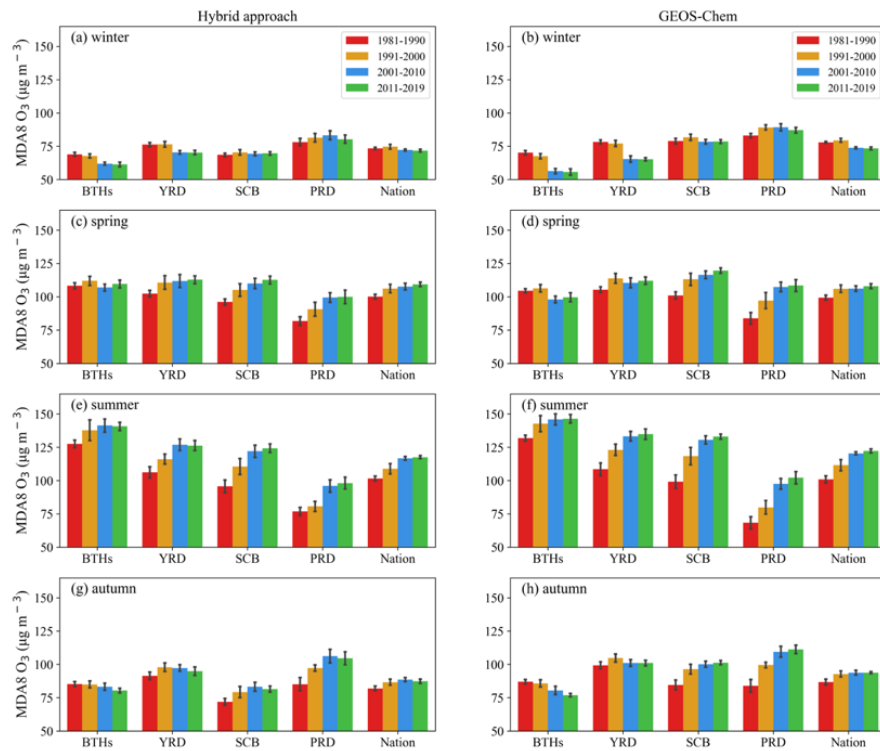
397

**Fig. 7** shows the bar plots of the seasonal MDA8-O<sub>3</sub> concentrations in each region from 1981–2019 for bias-corrected and GEOS-Chem-simulated O<sub>3</sub>. For the bias-corrected O<sub>3</sub>, the averaged summertime MDA8-O<sub>3</sub> concentrations in BTHs, YRD, SCB and fall-time MDA8-O<sub>3</sub> concentrations in PRD are  $137 \pm 8 \mu\text{g m}^{-3}$ ,  $119 \pm 10 \mu\text{g m}^{-3}$ ,  $113 \pm 12 \mu\text{g m}^{-3}$  and  $98 \pm 10 \mu\text{g m}^{-3}$ , with the increasing rate being  $0.46 \mu\text{g m}^{-3} \text{yr}^{-1}$ ,  $0.73 \mu\text{g m}^{-3} \text{yr}^{-1}$ ,  $0.98 \mu\text{g m}^{-3} \text{yr}^{-1}$  and  $0.69 \mu\text{g m}^{-3} \text{yr}^{-1}$  from 1981 to 2019, respectively (**Fig. S11**). For GEOS-Chem-simulated O<sub>3</sub>, the averaged summertime MDA8-O<sub>3</sub> concentrations in BTHs, YRD, SCB and fall-time MDA8-O<sub>3</sub> concentrations in PRD are  $141 \pm 7 \mu\text{g m}^{-3}$ ,  $125 \pm 11 \mu\text{g m}^{-3}$ ,  $120 \pm 14 \mu\text{g m}^{-3}$  and  $100 \pm 12 \mu\text{g m}^{-3}$ , respectively. It shows that O<sub>3</sub> concentrations of the four regions have a consistent upward trend in the summer over the past decades, but there are regional differences in other seasons. Compared to BTHs and YRD, PRD and SCB have more distinctive O<sub>3</sub> increases in spring and fall. Among these four regions, the O<sub>3</sub> concentrations in BTHs have the biggest seasonal differences, but have the smallest seasonal differences in PRD.

The spatiotemporal patterns of O<sub>3</sub> in China have been proven to largely depend on both emissions and meteorology. The regional O<sub>3</sub> pollution is usually found to be triggered by specific circulation patterns as local meteorological factors are modulated by synoptic-scale circulation patterns. China has a large territory and is affected by different weather systems. The continental high-pressure systems, components of East Asian summer monsoon (EASM) and tropical cyclones, among others, are critical synoptic conditions leading to O<sub>3</sub> formation and transport in China (Wang et al., 2022b; Han et al., 2020). For instance, regional O<sub>3</sub> pollution in North China usually occurs under a typical weather pattern of an anomalous high-pressure system at 500 hPa (Gong and Liao, 2019), which creates favorable meteorological conditions for high O<sub>3</sub> levels with high temperature, low relative humidity, anomalous southerlies and divergence in the lower troposphere. As one of the most important components of EASM, the Western Pacific subtropical high (WPSH) strongly influences summertime precipitation and atmospheric conditions in East China. A strong WPSH can decrease O<sub>3</sub> levels over YRD as enhanced moisture is transported into YRD under prevailing southwesterly winds (Zhao and Wang, 2017). Located on the southern coast of China, PRD features a typical subtropical monsoon climate. There O<sub>3</sub> concentrations are usually the lowest in summer due to the prevailing southerlies with clean air from the ocean and the associated large rainfall, while the worst O<sub>3</sub>

398 pollution usually happens in fall mainly due to the occasional northerly winds during the monsoonal transition, thereby  
 399 importing precursors from the north, and stable and still relatively warm and sunny weather conditions before the winter  
 400 starts. Downdrafts in the periphery circulation of a typhoon system can also strongly enhance surface O<sub>3</sub> before typhoon  
 401 landing (Jiang et al., 2015; Lu et al., 2021; Li et al., 2022). On one the hand, the poor ventilation in the peripheral subsidence  
 402 region of typhoons favors the accumulation of O<sub>3</sub> and its precursors. On the other hand, the deep subsidence can transport  
 403 the O<sub>3</sub> in the upper troposphere and lower stratosphere to surface, causing aggravated O<sub>3</sub> pollution. Moreover, smaller-  
 404 scale circulation patterns, such as land-sea and mountain-valley breezes, also influence O<sub>3</sub> in coastal regions (Ding et al.,  
 405 2004; Zhou et al., 2013; Wang et al., 2018a).

406 When compared to the hybrid approach, GEOS-Chem generally has similar O<sub>3</sub> distribution and trends over each  
 407 region, while overestimating O<sub>3</sub> concentrations (**Table S4**). GEOS-Chem particularly overestimates wintertime and fall-  
 408 time O<sub>3</sub> concentrations in SCB, which are  $10 \pm 1 \mu\text{g m}^{-3}$  and  $17 \pm 3 \mu\text{g m}^{-3}$  higher than those of the hybrid approach,  
 409 respectively. Previous studies reported such model overestimates and proposed a number of explanations involving  
 410 precursor emissions, dry deposition, and vertical mixing in the planetary boundary layer (PBL) (Lin et al., 2008; Travis et  
 411 al., 2016; Fiore et al., 2005). Both observational analyses and inter-model comparisons suggested that the summertime dry  
 412 deposition of O<sub>3</sub> calculated by the Wesely scheme in GEOS-Chem could be underestimated, which has been invoked as a  
 413 cause for model overestimates of O<sub>3</sub>. The biased emissions in the model, as consistent with the biased-high tropospheric  
 414 NO<sub>x</sub> columns, result in overestimated O<sub>3</sub>. Travis et al. (2016) showed that GEOS-Chem with reduced NO<sub>x</sub> emissions  
 415 provides an unbiased simulation of O<sub>3</sub> observations from the aircraft and reproduces the observed O<sub>3</sub> production efficiency  
 416 in the boundary layer. Lin et al. (2008) suggested that the excessive PBL mixing can lead to the biased-high O<sub>3</sub>  
 417 concentrations. The fully mixed O<sub>3</sub> throughout the PBL means that the higher O<sub>3</sub> concentrations in the upper PBL are  
 418 brought down to the surface much more efficiently. Moreover, the excessive spatial averaging of emissions at coarser  
 419 resolutions could also lead to systematic overestimation of regional O<sub>3</sub> production (Wild and Prather, 2006). In summary,  
 420 with a higher prediction accuracy, the hybrid approach lends greater credence to using model simulations to extrapolate  
 421 historical O<sub>3</sub> further back in time, which can furthermore provide us with more accurate estimates of O<sub>3</sub> impacts on crop  
 422 production and human health.

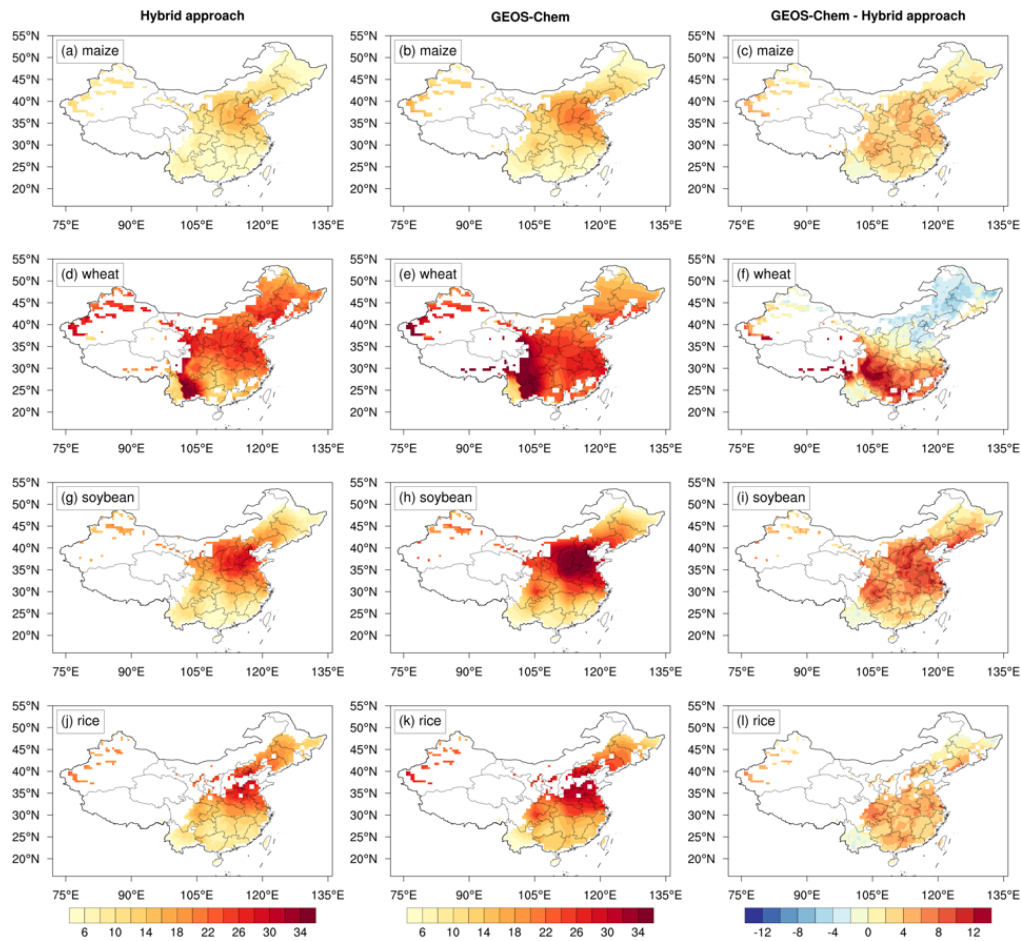


423

424 **Figure 7. The seasonal mean MDA8-O<sub>3</sub> concentrations ( $\mu\text{g m}^{-3}$ ) in different regions during 1981-2019. Bias-**  
 425 **corrected MDA8-O<sub>3</sub> in: (a) winter; (c) spring; (e) summer; and (g) fall. GEOS-Chem MDA8-O<sub>3</sub> in: (b) winter; (d)**  
 426 **spring; (f) summer; and (h) fall. The error bar represents the standard deviation.**

### 427 3.5 Crop production losses attributable to O<sub>3</sub> pollution

428 **Fig. 8** shows the relative yield losses (RYLs;  $\text{RYL} = 1 - \text{RY}$ , where RY is the relative yield defined as the ratio of the  
 429 O<sub>3</sub>-affected yield to the yield without O<sub>3</sub> exposure) calculated with GEOS-Chem and bias-corrected O<sub>3</sub> using AOT40-  
 430 China metric. For a given crop, the RYLs show generally consistent spatial distribution across the metrics, with BTHs  
 431 having the most serious crop yield losses due to high O<sub>3</sub> concentrations. Compared to the bias-corrected O<sub>3</sub>, using GEOS-  
 432 Chem-simulated O<sub>3</sub> generally leads to larger yield losses, especially over BTHs and SCB, reflecting overestimated O<sub>3</sub>  
 433 concentrations by GEOS-Chem in cropland areas during the growing seasons (**Fig. S12**), primarily in spring and summer,  
 434 which is consistent to the above analysis. GEOS-Chem-simulated O<sub>3</sub> leads to slightly underestimated wheat yield loss only  
 435 over some parts of BTHs, mostly because the primary growing period of wheat there is in winter and spring, and GEOS-  
 436 Chem has lower O<sub>3</sub> estimates than the hybrid approach during this period there (**Table S4**).



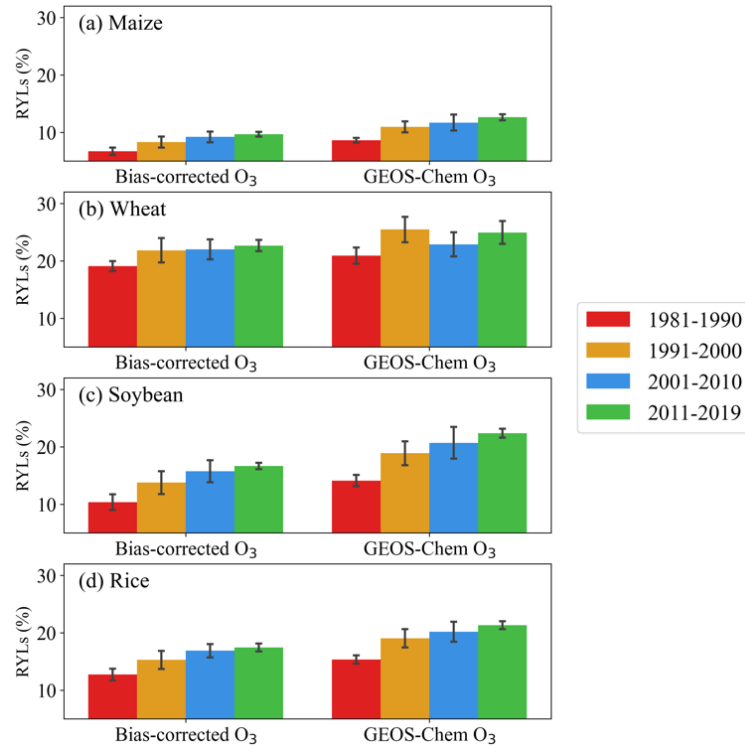
437 **Figure 8. Estimated annual mean relative yield losses (RYLs, in %) of four staple crops from 1981–2019 using the**  
 438 **AOT40-China metric. The estimated RYLs using bias-corrected O<sub>3</sub>: (a) maize; (d) wheat; (g) soybean; and (j) rice.**  
 439 **The estimated RYLs using GEOS-Chem-simulated O<sub>3</sub>: (b) maize; (e) wheat; (h) soybean; and (k) rice. The**  
 440 **differences in estimated RYLs between GEOS-Chem-simulated and bias-corrected O<sub>3</sub>: (c) maize; (f) wheat; (i)**  
 441 **soybean; and (l) rice. The GEOS-Chem-simulated O<sub>3</sub> were regridded to 0.5°×0.5° for comparison with bias-**  
 442 **corrected O<sub>3</sub>.**

444 **Fig. 9** shows the bar plots of the relative yield for each crop using AOT40-China exposure-yield response relationship.  
445 Crop yield losses are generally consistent with the O<sub>3</sub> trends as the exposure-yield relationships used here are essentially a  
446 set of linear functions. Most crops experience aggravated yield losses over the past four decades due to enhanced O<sub>3</sub>  
447 concentrations, except for wheat, which has the largest yield loss during the period 1991 to 2000. The reason could be that  
448 BTHs have the highest O<sub>3</sub> concentrations in spring during the 1990s, which is the primary growing season for wheat (**Fig.**  
449 **S13**). Noticeable uncertainties of crop yield losses are found across metrics.

450 The average annual crop RYLs from 1981 to 2019 for wheat, rice, soybean and maize range from 1.1 to 13.4%, 2.7 to  
451 13.4%, 6.3 to 24.8% and 0.8 to 7.4%, respectively. The differences in yield losses across crops reflect the dependence on  
452 crop-specific phenology and ecophysiology. The estimated annual RYLs using bias-corrected O<sub>3</sub> for wheat, rice, soybean  
453 and maize from 1981 to 2019 range from 17.5–25.5%, 10.7–19.1%, 7.3–17.9% and 7.1–12.7%, with a growth rate of 0.03%  
454 yr<sup>-1</sup>, 0.04% yr<sup>-1</sup>, 0.27% yr<sup>-1</sup> and 0.13% yr<sup>-1</sup>. Wheat is the most sensitive crop to the O<sub>3</sub> concentrations, whereas maize is  
455 the least sensitive. Using GEOS-Chem-simulated O<sub>3</sub>, the estimated annual RYLs for wheat, rice, soybean and maize from  
456 1981 to 2019 are 18.7–28.7%, 14.0–22.0%, 12.4–23.1%, and 7.9–13.2%, having a growth rate of 0.08% yr<sup>-1</sup>, 0.14% yr<sup>-1</sup>,  
457 0.23% yr<sup>-1</sup> and 0.11% yr<sup>-1</sup>. There are noticeable differences in crop yield estimates using the bias-corrected and GEOS-  
458 Chem O<sub>3</sub>, indicating again the importance of the bias-corrected high-resolution O<sub>3</sub> data in related crop issues.

459 In existing studies evaluating the O<sub>3</sub>-induced crop losses in China, which also use exposure-yield relationship derived  
460 from the experiments conducted in Asia, Zhang et al. (2017) reported that the ambient O<sub>3</sub> concentrations in Northeast China  
461 cause substantial annual yield loss of soybean ranging from 23.4% to 30.2% during 2013 and 2014, depending on the O<sub>3</sub>  
462 metric used (including AOT40, W126, SUM06 and a flux-based metric). Feng et al. (2022), using AOT40, indicated that  
463 the annual average RYLs of wheat (33%), rice (23%) and maize (9%) from 2017 to 2019. Our correspondingly estimated  
464 RYLs for rice (18.0%) and maize (10.0%) are generally consistent to their results, while the RYLs for soybean (16.4%)  
465 and wheat (23.4%) are much lower than the estimates. Since we used the same exposure-yield response relationships in  
466 their studies, the discrepancies are primarily attributed to the differences in used metrics (only for soybean), O<sub>3</sub> fields and  
467 sensitivity of crop to the changes of O<sub>3</sub> concentrations (Mukherjee et al., 2021; Feng et al., 2022; Mills et al., 2018). In  
468 Zhang et al. (2017), the O<sub>3</sub> measurements are obtained from the experimental field (45°73'N, 126°61'E), and in Feng et al.  
469 (2022), the measured O<sub>3</sub> concentrations are from over 3,000 monitoring sites across East Asia. The results of comparison  
470 are consistent to the previous analysis of O<sub>3</sub> trends and variability from different sources, where the domain-average values  
471 of O<sub>3</sub> observations are larger than gridded O<sub>3</sub> from model simulations (**Section 3.2**) and thus lead to larger estimates of  
472 RYLs. On one hand, it indicates that O<sub>3</sub> fields should be considered as a great source of uncertainty when comparing the  
473 results of previous studies using source-varied O<sub>3</sub> fields. Moreover, different degrees of importance should be given for  
474 specific crops, for example, the changes in O<sub>3</sub> concentrations have a larger impact on wheat crop. On the other hand, it  
475 highlights again the necessity and importance of bias correction for model-simulated O<sub>3</sub> when O<sub>3</sub>-induced crop reduction.





476

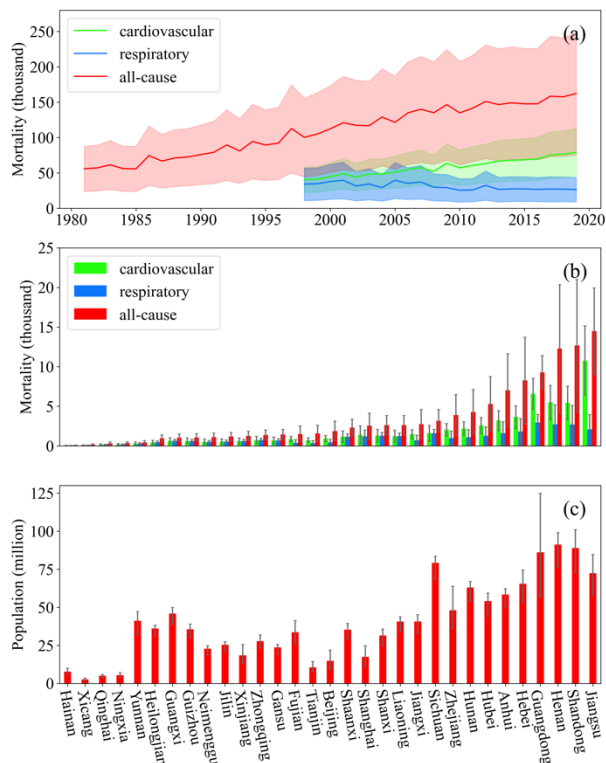
477 **Figure 9. The estimated decadal mean relative yield losses (RYLs) of four staple crops using different metrics from**  
 478 **1981–2019. The estimated RYLs using bias-corrected O<sub>3</sub>: (a) maize; (c) wheat; (e) soybean; and (g) rice. The**  
 479 **estimated RYLs using GEOS-Chem-simulated O<sub>3</sub>: (b) maize; (d) wheat; (f) soybean; and (h) rice. The error bar**  
 480 **represents the standard deviation.**

481 **3.6 Health impacts attributable to O<sub>3</sub> pollution**

482 The estimated annual all-cause premature deaths induced by O<sub>3</sub> increase from 55,876 in 1981 to 162,370 in 2019 with  
 483 an increasing trend of +2,979 deaths yr<sup>-1</sup>. The annual premature deaths related to respiratory and cardiovascular diseases  
 484 are 34,155 and 40,323 in 1998, and 26,471 and 79,021 in 2019, having a rate of change of -546 and +1,773 deaths yr<sup>-1</sup>  
 485 during 1998–2019, respectively (**Fig. 10a**). Among three types of health outcomes, only respiratory diseases experienced  
 486 a decreasing trend in premature mortality, and the premature mortality is constantly below 40,000. The decreasing trend of  
 487 the respiration-related mortality primarily results from the decreased annual baseline mortality rate over the past decades  
 488 (**Fig. S14**). As the total respiratory-related deaths decreased over the past decades, respiratory O<sub>3</sub> deaths are decreasing  
 489 even under aggravated O<sub>3</sub> pollution. Based on GEOS-Chem-simulated O<sub>3</sub>, the corresponding estimated change rate for all-  
 490 cause disease is +3,516 deaths yr<sup>-1</sup> from 50,384 in 1981 to 176,741 in 2019. Premature mortality induced by respiratory  
 491 disease decreases from 37,822 in 1998 to 29,079 in 2019 with a change rate of -584 deaths yr<sup>-1</sup>, while cardiovascular  
 492 disease increases from 44,516 in 1998 to 85,980 in 2019 with a change rate of +1,977 deaths yr<sup>-1</sup> (**Fig. S15**). The result  
 493 shows that using GEOS-Chem-simulated O<sub>3</sub> generally gives higher estimates of mortality than using the bias-corrected  
 494 data. **Fig. 10b** shows the provincial annual average premature mortality of different health endpoints. The five provinces  
 495 with the highest all-cause mortality are Jiangsu [14,510 (95% CI: 9,022–19,935)], Shandong [12,684 (95% CI: 4,258–  
 496 20,990)], Henan [12,290 (95% CI: 4,125–20,343)], Guangdong [9,268 (95% CI: 7,224–11,416)] and Hebei [8,276 (95%  
 497 CI: 2,776–13,706)], which are generally consistent with previous studies for China (Zhang et al., 2021; Zhang et al., 2022a).  
 498 Similar distribution can be found for respiratory and cardiovascular diseases but with a different ranking order. Generally,  
 499 those provinces in densely populated areas (**Fig. 10c**) with higher O<sub>3</sub> concentrations, such as BTHs, YRD and PRD, have  
 500 higher health burdens. In contrast, the northeastern and southern China (excluding Guangdong) suffer the least life losses

501 induced by O<sub>3</sub> exposure (**Fig. S16**).

502 When compared with estimates from previous studies, our estimates of are generally quite consistent with that given  
503 by Maji and Namdeo (2021), which reported that the short-term all-cause, cardiovascular and respiratory premature  
504 mortalities attributed to ambient O<sub>3</sub> exposure were 156,000, 73,500 and 28,600 in 2019. Based on O<sub>3</sub> observations in 334  
505 Chinese cities, Zhang et al. (2021) suggested that the national all-cause, respiratory, cardiovascular mortalities attributable  
506 to O<sub>3</sub> are 270,000 to 390,000, 49,000 to 63,000, and 150,000 to 220,000 across 2015–2018, which are much higher than  
507 most existing results. Since the methodological approaches are largely similar and we use the log-linear exposure-response  
508 function, we ascribe that the very high estimated mortalities are mainly due to concentration–response threshold  $X_0$  assumed  
509 to be zero in their study. A lower  $X_0$  means that O<sub>3</sub> can cause more adverse impacts on human health even at low  
510 concentrations, thus leading to higher mortalities.



511 **Figure 10. (a) Annual premature mortality (thousand) for different diseases over the past decades; (b) annual mean**  
512 **province-based mortality (thousand) attributed to different health endpoints; and (c) annual mean province-based**  
513 **population (million). The mortality is calculated using the bias-corrected O<sub>3</sub>.**  
514

#### 515 4. Conclusions and discussion

516 In this study, to have a more accurate characterization of O<sub>3</sub> spatiotemporal distribution and trends as well as their  
517 impacts on agriculture and human health, we used a hybrid approach to generate bias-corrected O<sub>3</sub> data across China from  
518 1981 to 2019. The hybrid approach helps improve O<sub>3</sub> predictions by taking advantage of a chemical transport model, a ML  
519 algorithm and increasing availability of high-resolution environmental and meteorological data. In the model training  
520 process, we found that utilizing a higher-resolution meteorological dataset, albeit one that is not the same as the default  
521 CTM input meteorology, has high potential to enhance the performance of the hybrid model in reproducing observed O<sub>3</sub>  
522 concentrations. The validation shows that the bias-corrected O<sub>3</sub> can achieve a higher prediction accuracy than GEOS-  
523 Chem-simulated O<sub>3</sub> alone when compared with historical in-situ measurements. Before being corrected, the GEOS-  
524 Chem-simulated O<sub>3</sub> concentrations tend to be overestimated and lead to higher crop yield losses and larger O<sub>3</sub>-induced mortalities.

525 Noticeable differences in crop RYLs and mortality estimates highlight the advantages of using high-resolution O<sub>3</sub> data to  
526 improve our understanding of long-term O<sub>3</sub> impacts.

527 When examining the regional and national O<sub>3</sub> trends, we found that MDA8-O<sub>3</sub> concentrations have a perceptible  
528 increasing trend before 2000s, but fluctuate within a certain range with large interannual variabilities in more recent years.  
529 The large discrepancies in previous studies indicate that the regional and national O<sub>3</sub> trends in China still suffer with great  
530 uncertainties, particularly when different approaches are used to produce the O<sub>3</sub> estimates. However, these studies using  
531 source-varied O<sub>3</sub> fields consistently show the great interannual variabilities of O<sub>3</sub> concentrations. Some insights can be  
532 obtained from existing findings, which need to be carefully considered when examining O<sub>3</sub> trends and comparing them  
533 with existing results. First, given the large site differences, the calculation of observational O<sub>3</sub> trends is very sensitive to  
534 the subsets of data from networks. Thus, great uncertainty could still exist even using O<sub>3</sub> observations from the same source  
535 depending on the chosen subsets of data. Second, different formats of O<sub>3</sub> fields (e.g., site-based and gridded) could lead to  
536 large uncertainties of the O<sub>3</sub> trend estimates. A higher resolution of gridded O<sub>3</sub> estimates from CTMs and ML may reduce  
537 the differences between O<sub>3</sub> observational results. Third, the calculated O<sub>3</sub> trends are very sensitive to the chosen study  
538 period due to large interannual variability and seasonal differences. The changing meteorological conditions are the major  
539 factor causing the large interannual O<sub>3</sub> variations, and reductions in the emissions of NO<sub>x</sub>, SO<sub>2</sub> and PM also have complex  
540 effects on ground-level O<sub>3</sub> concentrations (Wang et al., 2022b). Liu and Wang (2020a) suggested that the meteorological  
541 impacts on O<sub>3</sub> trends vary region by region and year by year and could be comparable with or even larger than the impacts  
542 of changes in anthropogenic emissions.

543 Our estimated RYLs for maize and rice and soybean in China are generally consistent to existing studies, while the  
544 RYLs for soybean and wheat are lower than their estimates mainly due to the differences in used metrics, O<sub>3</sub> fields and  
545 crop sensitivity to ambient O<sub>3</sub> concentrations. It suggests that plating O<sub>3</sub>-resistant cultivars could be an effective approach  
546 to increase total crop production to meet the increasing food demands. In addition to the metrics and O<sub>3</sub> fields, uncertainties  
547 of estimated O<sub>3</sub>-induced crop losses could be also from other sources (e.g., exposure-yield relationships). Though some  
548 other metrics (e.g., M7/M12 and W126) have also been used in some studies (Van Dingenen et al., 2009; Avnery et al.,  
549 2013; Wang et al., 2022c), there are not available exposure-yield relationships for all four major crops specific for China.  
550 The estimated RYLs for crops could be largely biased using metrics with exposure-yield relationships developed for U.S.  
551 or Europe (**Fig. S17**), as they are inadequate to represent Asian crop genotypes and environmental conditions. So, the  
552 region-specific exposure-yield relationships are highly recommended to be used in future study estimating the O<sub>3</sub>-induced  
553 crop reduction, especially for the regional study.

554 In recent years, although existing studies have made efforts to quantify the O<sub>3</sub>-related health impacts in China, only a  
555 few focused on the nationwide acute O<sub>3</sub> health burden assessment, particularly for assessment over multiple decades (Maji  
556 and Namdeo, 2021; Sahu et al., 2021; Zhang et al., 2021; Zhang et al., 2022a). There are some remaining issues to be  
557 addressed regarding O<sub>3</sub> health impacts. For instance, the existence of a “safe” threshold of O<sub>3</sub> levels still remains debated.  
558 A recent study reported that no consistent evidence was found for a threshold in the O<sub>3</sub>-mortality concentration-response  
559 relationship in seven cities of Jiangsu Province, China during 2013–2014 (Chen et al., 2017; Maji and Namdeo, 2021).  
560 Given the importance of the threshold assumption in assessing health effects of air pollution, more studies are needed to  
561 determine a most likely threshold for O<sub>3</sub>-mortality association in the future. Moreover, the multiple temporal O<sub>3</sub> metrics  
562 (e.g., 1-h maximum and daytime average O<sub>3</sub> concentrations) have also been proved to play an important role in the  
563 variability of estimated health effects, even though standard ratios are used to convert among multiple metrics (Anderson  
564 and Bell, 2010). In addition to the uncertainties from varying methodologies, interpretation of the O<sub>3</sub> epidemiological  
565 impact is also constrained by the variability in geographical, seasonal, and demographic characteristics (Yin et al., 2017b).  
566 Liu et al. (2013) suggested that associations between O<sub>3</sub> and mortality appeared to be more evident during the cool season  
567 than in the warm season, and stronger in the oldest age group and among those with less education. The effect modification

568 by population susceptibility and the confounding effects of concomitant exposures (temperature, particulate matter, etc.)  
569 should be further considered in future works.

570 A major limitation of our study lies in the uncertain predictions in regions where monitoring data are scarce (e.g., the  
571 western half of China). The monitoring sites are sparsely distributed in those areas, which may fail to capture the accurate  
572 association between O<sub>3</sub> concentrations and various predictors there, especially considering that the ML algorithm has likely  
573 over-emphasized such relationships in the data-intensive eastern regions. Second, the land use data were prescribed in 2013  
574 due to the limited availability of data, and this may neglect some major land use changes in China over the past decades.  
575 Though the land use data were found by the ML algorithm to contribute little to the overall model, more detailed land use  
576 data are expected to further increase model accuracy. In addition, though concentration-based metrics are easy to calculate  
577 and ensured to be scientifically sound in some experiments (Fuhrer et al., 1997; Mills et al., 2007), they do not consider  
578 the active responses of plant ecophysiology to ambient climatic and environmental changes and thus likely inadequate for  
579 examining yield losses in a future climate and atmospheric environment (Tai et al., 2021). So, flux-based metrics are  
580 recommended in future studies to better understand the long-term evolution of crop losses over China (Feng et al., 2012;  
581 Zhang et al., 2017; Tai et al., 2021; Pleijel et al., 2022), wherein more crop- and region-specific experiments and trials are  
582 needed to acquire appropriate metrics and exposure-yield response functions and calibrate the process-based crop model.

583 Despite these limitations, our study represents important progress in evaluating the long-term, multidecadal health  
584 burdens and agricultural losses resulting from O<sub>3</sub> pollution in China. Across the four major regions, BTHs experience the  
585 highest RYLs for major crops due to elevated O<sub>3</sub>. On the other hand, the YRD and PRD regions have greater human health  
586 losses primarily due to their large population size. The results can provide important references for governments and  
587 agencies when making related national or regional policies to meet the imperative environment, health, and food security  
588 demands. To effectively address O<sub>3</sub> impacts, collaborative efforts can be made in multifaceted aspects: (1) to implement  
589 stricter regulations and specific emission control measures for major ozone precursors from industrial, vehicular and  
590 agricultural sources that account for region-specific chemical, meteorological and terrestrial conditions; (2) to encourage  
591 the adoption of more sustainable and adaptive agricultural practices that minimize O<sub>3</sub> exposure and its damage on crops  
592 (e.g., cultivating O<sub>3</sub>-resistant crop varieties); (3) to improve short-range O<sub>3</sub> forecast capabilities of regional models,  
593 especially with the enhancement of artificial intelligence technology, which may enable better early warning systems to  
594 prepare the public and farmers for O<sub>3</sub> episodes; (4) to raise public awareness via promotional campaigns and educational  
595 programs to inform individuals, communities, and farmers about the risks associated with O<sub>3</sub>. It is important for  
596 policymakers to consider these suggestions and act to effectively mitigate the negative O<sub>3</sub> impacts.

597 **Data availability.** Model output data used for analysis and plotting are available on the open-access online repository:  
598 [ml\\_simulated\\_ozone\\_China](#).

599 **Competing interests.** The authors declare that neither they nor their co-authors have any competing interests. At least one  
600 of the (co-)authors is a member of the editorial board of Atmospheric Chemistry and Physics.

601 **Author contributions.** APKT designed the study and supervised the writing of the paper. JM conducted model simulation,  
602 analyzed results, and wrote the draft with the assistance of TGY and KTC. DHYY performed the GEOS-Chem simulations.  
603 ZZF assisted in the interpretation of the results. All authors contributed to the discussion and improvement of the paper.

604 **Acknowledgements.** This work was supported by the National Natural Science Foundation of China (NSFC)/Research  
605 Grants Council (RGC) Joint Research Scheme (reference #: N\_CUHK440/20, 42061160479) awarded to A. P. K. Tai and  
606 Z. Feng.

607 **References**

- 608 Abdullah, S., Ismail, M., and Fong, S. Y.: Multiple Linear Regression (MLR) models for long term PM10 concentration  
609 forecasting during different monsoon seasons, *Journal of Sustainability Science and Management*, 12, 60-69, 2017.
- 610 Accadia, C., Mariani, S., Casaioli, M., Lavagnini, A., and Speranza, A.: Sensitivity of Precipitation Forecast Skill Scores  
611 to Bilinear Interpolation and a Simple Nearest-Neighbor Average Method on High-Resolution Verification Grids,  
612 *Weather and Forecasting*, 18, 918-932, [https://doi.org/10.1175/1520-0434\(2003\)018<0918:SOPFSS>2.0.CO;2](https://doi.org/10.1175/1520-0434(2003)018<0918:SOPFSS>2.0.CO;2), 2003.
- 613 Anderson, G. B. and Bell, M. L.: Does one size fit all? The suitability of standard ozone exposure metric conversion ratios  
614 and implications for epidemiology, *Journal of Exposure Science & Environmental Epidemiology*, 20, 2-11,  
615 <https://doi.org/10.1038/jes.2008.69>, 2010.
- 616 Avnery, S., Mauzerall, D. L., and Fiore, A. M.: Increasing global agricultural production by reducing ozone damages via  
617 methane emission controls and ozone-resistant cultivar selection, *Global Change Biology*, 19, 1285-1299,  
618 <https://doi.org/10.1111/gcb.12118>, 2013.
- 619 Bey, I., Jacob, D. J., Yantosca, R. M., Logan, J. A., Field, B. D., Fiore, A. M., Li, Q., Liu, H. Y., Mickley, L. J., and Schultz,  
620 M. G.: Global modeling of tropospheric chemistry with assimilated meteorology: Model description and evaluation,  
621 *Journal of Geophysical Research: Atmospheres*, 106, 23073-23095, <https://doi.org/10.1029/2001JD000807>, 2001.
- 622 Bi, J., Knowland, K. E., Keller, C. A., and Liu, Y.: Combining Machine Learning and Numerical Simulation for High-  
623 Resolution PM2.5 Concentration Forecast, *Environ Sci Technol*, 56, 1544-1556,  
624 <https://doi.org/10.1021/acs.est.1c05578>, 2022.
- 625 Chen, K., Zhou, L., Chen, X., Bi, J., and Kinney, P. L.: Acute effect of ozone exposure on daily mortality in seven cities of  
626 Jiangsu Province, China: No clear evidence for threshold, *Environmental Research*, 155, 235-241,  
627 <https://doi.org/10.1016/j.envres.2017.02.009>, 2017.
- 628 Chen, T. and Guestrin, C.: XGBoost: A Scalable Tree Boosting System, *Proceedings of the 22nd ACM SIGKDD  
629 International Conference on Knowledge Discovery and Data Mining*, San Francisco, California, USA,  
630 <https://doi.org/10.1145/2939672.2939785>, 2016.
- 631 Clifton, O. E., Fiore, A. M., Massman, W. J., Baublitz, C. B., Coyle, M., Emberson, L., Fares, S., Farmer, D. K., Gentine,  
632 P., Gerosa, G., Guenther, A. B., Helmig, D., Lombardozi, D. L., Munger, J. W., Patton, E. G., Pusede, S. E., Schwede,  
633 D. B., Silva, S. J., Sorgel, M., Steiner, A. L., and Tai, A. P. K.: Dry Deposition of Ozone over Land: Processes,  
634 Measurement, and Modeling, *Rev Geophys*, 58, <https://doi.org/10.1029/2019RG000670>, 2020.
- 635 Dang, R., Liao, H., and Fu, Y.: Quantifying the anthropogenic and meteorological influences on summertime surface ozone  
636 in China over 2012–2017, *Science of The Total Environment*, 754, 142394,  
637 <https://doi.org/10.1016/j.scitotenv.2020.142394>, 2021.
- 638 Dedoussi, I. C., Eastham, S. D., Monier, E., and Barrett, S. R. H.: Premature mortality related to United States cross-state  
639 air pollution, *Nature*, 578, 261-265, <https://doi.org/10.1038/s41586-020-1983-8>, 2020.
- 640 Di, Q., Rowland, S., Koutrakis, P., and Schwartz, J.: A hybrid model for spatially and temporally resolved ozone exposures  
641 in the continental United States, *Journal of the Air & Waste Management Association*, 67, 39-52,  
642 <https://doi.org/10.1080/10962247.2016.1200159>, 2017.
- 643 Ding, A., Wang, T., Zhao, M., Wang, T., and Li, Z.: Simulation of sea-land breezes and a discussion of their implications  
644 on the transport of air pollution during a multi-day ozone episode in the Pearl River Delta of China, *Atmospheric  
645 Environment*, 38, 6737-6750, <https://doi.org/10.1016/j.atmosenv.2004.09.017>, 2004.
- 646 Emberson, L. D., Büker, P., Ashmore, M. R., Mills, G., Jackson, L. S., Agrawal, M., Atikuzzaman, M. D., Cinderby, S.,  
647 Engardt, M., Jamir, C., Kobayashi, K., Oanh, N. T. K., Quadir, Q. F., and Wahid, A.: A comparison of North American  
648 and Asian exposure–response data for ozone effects on crop yields, *Atmospheric Environment*, 43, 1945-1953,  
649 <https://doi.org/10.1016/j.atmosenv.2009.01.005>, 2009.
- 650 Feng, Z., Calatayud, V., Zhu, J., and Kobayashi, K.: Ozone exposure- and flux-based response relationships with

651 photosynthesis of winter wheat under fully open air condition, *Science of The Total Environment*, 619-620, 1538-  
652 1544, <https://doi.org/10.1016/j.scitotenv.2017.10.089>, 2018.

653 Feng, Z., Tang, H., Uddling, J., Pleijel, H., Kobayashi, K., Zhu, J., Oue, H., and Guo, W.: A stomatal ozone flux–response  
654 relationship to assess ozone-induced yield loss of winter wheat in subtropical China, *Environmental Pollution*, 164,  
655 16-23, <https://doi.org/10.1016/j.envpol.2012.01.014>, 2012.

656 Feng, Z., De Marco, A., Anav, A., Gualtieri, M., Sicard, P., Tian, H., Fornasier, F., Tao, F., Guo, A., and Paoletti, E.:  
657 Economic losses due to ozone impacts on human health, forest productivity and crop yield across China, *Environ Int*,  
658 131, 104966, <https://doi.org/10.1016/j.envint.2019.104966>, 2019.

659 Feng, Z., Xu, Y., Kobayashi, K., Dai, L., Zhang, T., Agathokleous, E., Calatayud, V., Paoletti, E., Mukherjee, A., Agrawal,  
660 M., Park, R. J., Oak, Y. J., and Yue, X.: Ozone pollution threatens the production of major staple crops in East Asia,  
661 *Nature Food*, 3, 47-56, <https://doi.org/10.1038/s43016-021-00422-6>, 2022.

662 Fiore, A. M., Horowitz, L. W., Purves, D. W., Levy Ii, H., Evans, M. J., Wang, Y., Li, Q., and Yantosca, R. M.: Evaluating  
663 the contribution of changes in isoprene emissions to surface ozone trends over the eastern United States, *Journal of*  
664 *Geophysical Research: Atmospheres*, 110, <https://doi.org/10.1029/2004JD005485>, 2005.

665 Fu, Y. and Tai, A. P. K.: Impact of climate and land cover changes on tropospheric ozone air quality and public health in  
666 East Asia between 1980 and 2010, *Atmos. Chem. Phys.*, 15, 10093-10106, <https://doi.org/10.5194/acp-15-10093-2015>,  
667 2015.

668 Fuhrer, J., Skärby, L., and Ashmore, M. R.: Critical levels for ozone effects on vegetation in Europe, *Environmental*  
669 *Pollution*, 97, 91-106, [https://doi.org/10.1016/S0269-7491\(97\)00067-5](https://doi.org/10.1016/S0269-7491(97)00067-5), 1997.

670 Fusco, A. C. and Logan, J. A.: Analysis of 1970–1995 trends in tropospheric ozone at Northern Hemisphere midlatitudes  
671 with the GEOS-CHEM model, *Journal of Geophysical Research: Atmospheres*, 108,  
672 <https://doi.org/10.1029/2002JD002742>, 2003.

673 Gong, C. and Liao, H.: A typical weather pattern for ozone pollution events in North China, *Atmos. Chem. Phys.*, 19,  
674 13725-13740, <https://doi.org/10.5194/acp-19-13725-2019>, 2019.

675 Gong, C., Yue, X., Liao, H., and Ma, Y.: A humidity-based exposure index representing ozone damage effects on vegetation,  
676 *Environmental Research Letters*, 16, <https://doi.org/10.1088/1748-9326/abecbb>, 2021.

677 Guenther, A. B., Jiang, X., Heald, C. L., Sakulyanontvittaya, T., Duhl, T., Emmons, L. K., and Wang, X.: The Model of  
678 Emissions of Gases and Aerosols from Nature version 2.1 (MEGAN2.1): an extended and updated framework for  
679 modeling biogenic emissions, *Geosci. Model Dev.*, 5, 1471-1492, <https://doi.org/10.5194/gmd-5-1471-2012>, 2012.

680 Han, H., Liu, J., Shu, L., Wang, T., and Yuan, H.: Local and synoptic meteorological influences on daily variability in  
681 summertime surface ozone in eastern China, *Atmos. Chem. Phys.*, 20, 203-222, [https://doi.org/10.5194/acp-20-203-](https://doi.org/10.5194/acp-20-203-2020)  
682 [2020](https://doi.org/10.5194/acp-20-203-2020), 2020.

683 He, J., Wang, Y., Hao, J., Shen, L., and Wang, L.: Variations of surface O<sub>3</sub> in August at a rural site near Shanghai: influences  
684 from the West Pacific subtropical high and anthropogenic emissions, *Environmental Science and Pollution Research*,  
685 19, 4016-4029, <https://doi.org/10.1007/s11356-012-0970-5>, 2012.

686 Hoesly, R. M., Smith, S. J., Feng, L., Klimont, Z., Janssens-Maenhout, G., Pitkanen, T., Seibert, J. J., Vu, L., Andres, R. J.,  
687 Bolt, R. M., Bond, T. C., Dawidowski, L., Kholod, N., Kurokawa, J. I., Li, M., Liu, L., Lu, Z., Moura, M. C. P.,  
688 O'Rourke, P. R., and Zhang, Q.: Historical (1750–2014) anthropogenic emissions of reactive gases and aerosols from  
689 the Community Emissions Data System (CEDS), *Geosci. Model Dev.*, 11, 369-408, [https://doi.org/10.5194/gmd-11-](https://doi.org/10.5194/gmd-11-369-2018)  
690 [369-2018](https://doi.org/10.5194/gmd-11-369-2018), 2018.

691 Hu, X., Belle, J. H., Meng, X., Wildani, A., Waller, L. A., Strickland, M. J., and Liu, Y.: Estimating PM<sub>2.5</sub> Concentrations  
692 in the Conterminous United States Using the Random Forest Approach, *Environ Sci Technol*, 51, 6936-6944,  
693 <https://doi.org/10.1021/acs.est.7b01210>, 2017.

694 Irrgang, C., Boers, N., Sonnewald, M., Barnes, E. A., Kadow, C., Staneva, J., and Saynisch-Wagner, J.: Towards neural

695 Earth system modelling by integrating artificial intelligence in Earth system science, *Nature Machine Intelligence*, 3,  
696 667-674, <https://doi.org/10.1038/s42256-021-00374-3>, 2021.

697 Ivatt, P. D. and Evans, M. J.: Improving the prediction of an atmospheric chemistry transport model using gradient-boosted  
698 regression trees, *Atmos. Chem. Phys.*, 20, 8063-8082, <https://doi.org/10.5194/acp-20-8063-2020>, 2020.

699 Jacob, D. J. and Winner, D. A.: Effect of climate change on air quality, *Atmospheric Environment*, 43, 51-63,  
700 <https://doi.org/10.1016/j.atmosenv.2008.09.051>, 2009.

701 Jiang, Y. C., Zhao, T. L., Liu, J., Xu, X. D., Tan, C. H., Cheng, X. H., Bi, X. Y., Gan, J. B., You, J. F., and Zhao, S. Z.: Why  
702 does surface ozone peak before a typhoon landing in southeast China?, *Atmos. Chem. Phys.*, 15, 13331-13338,  
703 <https://doi.org/10.5194/acp-15-13331-2015>, 2015.

704 Kawase, H., Nagashima, T., Sudo, K., and Nozawa, T.: Future changes in tropospheric ozone under Representative  
705 Concentration Pathways (RCPs), *Geophysical Research Letters*, 38, <https://doi.org/10.1029/2010GL046402>, 2011.

706 Lelieveld, J., Evans, J. S., Fnais, M., Giannadaki, D., and Pozzer, A.: The contribution of outdoor air pollution sources to  
707 premature mortality on a global scale, *Nature*, 525, 367-371, <https://doi.org/10.1038/nature15371>, 2015.

708 Li, K., Jacob, D. J., Shen, L., Lu, X., De Smedt, I., and Liao, H.: Increases in surface ozone pollution in China from 2013  
709 to 2019: anthropogenic and meteorological influences, *Atmos. Chem. Phys.*, 20, 11423-11433,  
710 <https://doi.org/10.5194/acp-20-11423-2020>, 2020.

711 Li, K., Jacob, D. J., Liao, H., Qiu, Y., Shen, L., Zhai, S., Bates, K. H., Sulprizio, M. P., Song, S., Lu, X., Zhang, Q., Zheng,  
712 B., Zhang, Y., Zhang, J., Lee, H. C., and Kuk, S. K.: Ozone pollution in the North China Plain spreading into the late-  
713 winter haze season, *Proceedings of the National Academy of Sciences*, 118, e2015797118, 10.1073/pnas.2015797118,  
714 2021.

715 Li, Y., Zhao, X., Deng, X., and Gao, J.: The impact of peripheral circulation characteristics of typhoon on sustained ozone  
716 episodes over the Pearl River Delta region, China, *Atmos. Chem. Phys.*, 22, 3861-3873, <https://doi.org/10.5194/acp-22-3861-2022>, 2022.

718 Lin, J. T., Youn, D., Liang, X. Z., and Wuebbles, D. J.: Global model simulation of summertime U.S. ozone diurnal cycle  
719 and its sensitivity to PBL mixing, spatial resolution, and emissions, *Atmospheric Environment*, 42, 8470-8483,  
720 <https://doi.org/10.1016/j.atmosenv.2008.08.012>, 2008.

721 Liu, H., Liu, S., Xue, B., Lv, Z., Meng, Z., Yang, X., Xue, T., Yu, Q., and He, K.: Ground-level ozone pollution and its  
722 health impacts in China, *Atmospheric Environment*, 173, 223-230, <https://doi.org/10.1016/j.atmosenv.2017.11.014>,  
723 2018.

724 Liu, J., Wang, L., Li, M., Liao, Z., Sun, Y., Song, T., Gao, W., Wang, Y., Li, Y., Ji, D., Hu, B., Kerminen, V. M., Wang, Y.,  
725 and Kulmala, M.: Quantifying the impact of synoptic circulation patterns on ozone variability in northern China from  
726 April to October 2013–2017, *Atmos. Chem. Phys.*, 19, 14477-14492, <https://doi.org/10.5194/acp-19-14477-2019>,  
727 2019.

728 Liu, R., Ma, Z., Liu, Y., Shao, Y., Zhao, W., and Bi, J.: Spatiotemporal distributions of surface ozone levels in China from  
729 2005 to 2017: A machine learning approach, *Environ Int*, 142, 105823, <https://doi.org/10.1016/j.envint.2020.105823>,  
730 2020.

731 Liu, T., Li, T. T., Zhang, Y. H., Xu, Y. J., Lao, X. Q., Rutherford, S., Chu, C., Luo, Y., Zhu, Q., Xu, X. J., Xie, H. Y., Liu,  
732 Z. R., and Ma, W. J.: The short-term effect of ambient ozone on mortality is modified by temperature in Guangzhou,  
733 China, *Atmospheric Environment*, 76, 59-67, <https://doi.org/10.1016/j.atmosenv.2012.07.011>, 2013.

734 Liu, Y. and Wang, T.: Worsening urban ozone pollution in China from 2013 to 2017 – Part 1: The complex and varying  
735 roles of meteorology, *Atmos. Chem. Phys.*, 20, 6305-6321, <https://doi.org/10.5194/acp-20-6305-2020>, 2020a.

736 Liu, Y. and Wang, T.: Worsening urban ozone pollution in China from 2013 to 2017 – Part 2: The effects of emission  
737 changes and implications for multi-pollutant control, *Atmos. Chem. Phys.*, 20, 6323-6337,  
738 <https://doi.org/10.5194/acp-20-6323-2020>, 2020b.

739 Lu, C., Mao, J., Wang, L., Guan, Z., Zhao, G., and Li, M.: An unusual high ozone event over the North and Northeast China  
740 during the record-breaking summer in 2018, *J Environ Sci (China)*, 104, 264-276,  
741 <https://doi.org/10.1016/j.jes.2020.11.030>, 2021.

742 Lu, X., Hong, J., Zhang, L., Cooper, O. R., Schultz, M. G., Xu, X., Wang, T., Gao, M., Zhao, Y., and Zhang, Y.: Severe  
743 Surface Ozone Pollution in China: A Global Perspective, *Environmental Science & Technology Letters*, 5, 487-494,  
744 <https://doi.org/10.1021/acs.estlett.8b00366>, 2018.

745 Lu, X., Zhang, L., Chen, Y., Zhou, M., Zheng, B., Li, K., Liu, Y., Lin, J., Fu, T.-M., and Zhang, Q.: Exploring 2016–2017  
746 surface ozone pollution over China: source contributions and meteorological influences, *Atmos. Chem. Phys.*, 19,  
747 8339-8361, <https://doi.org/10.5194/acp-19-8339-2019>, 2019.

748 Ma, R., Ban, J., Wang, Q., Zhang, Y., Yang, Y., He, M. Z., Li, S., Shi, W., and Li, T.: Random forest model based fine scale  
749 spatiotemporal O<sub>3</sub> trends in the Beijing-Tianjin-Hebei region in China, 2010 to 2017, *Environmental Pollution*, 276,  
750 116635, <https://doi.org/10.1016/j.envpol.2021.116635>, 2021.

751 Madaniyazi, L., Nagashima, T., Guo, Y., Pan, X., and Tong, S.: Projecting ozone-related mortality in East China,  
752 *Environment International*, 92-93, 165-172, <https://doi.org/10.1016/j.envint.2016.03.040>, 2016.

753 Maji, K. J. and Namdeo, A.: Continuous increases of surface ozone and associated premature mortality growth in China  
754 during 2015–2019, *Environmental Pollution*, 269, 116183, <https://doi.org/10.1016/j.envpol.2020.116183>, 2021.

755 Mao, J., Wang, L., Lu, C., Liu, J., Li, M., Tang, G., Ji, D., Zhang, N., and Wang, Y.: Meteorological mechanism for a large-  
756 scale persistent severe ozone pollution event over eastern China in 2017, *J Environ Sci (China)*, 92, 187-199,  
757 <https://doi.org/10.1016/j.jes.2020.02.019>, 2020.

758 Mills, G., Buse, A., Gimeno, B., Bermejo, V., Holland, M., Emberson, L., and Pleijel, H.: A synthesis of AOT40-based  
759 response functions and critical levels of ozone for agricultural and horticultural crops, *Atmospheric Environment*, 41,  
760 2630-2643, <https://doi.org/10.1016/j.atmosenv.2006.11.016>, 2007.

761 Mills, G., Sharps, K., Simpson, D., Pleijel, H., Frei, M., Burkey, K., Emberson, L., Uddling, J., Broberg, M., Feng, Z.,  
762 Kobayashi, K., and Agrawal, M.: Closing the global ozone yield gap: Quantification and cobenefits for multistress  
763 tolerance, *Global Change Biology*, 24, 4869-4893, <https://doi.org/10.1111/gcb.14381>, 2018.

764 Monfreda, C., Ramankutty, N., and Foley, J. A.: Farming the planet: 2. Geographic distribution of crop areas, yields,  
765 physiological types, and net primary production in the year 2000, *Global Biogeochemical Cycles*, 22,  
766 <https://doi.org/10.1029/2007GB002947>, 2008.

767 Moustris, K. P., Nastos, P. T., Larissi, I. K., and Paliatsos, A. G.: Application of Multiple Linear Regression Models and  
768 Artificial Neural Networks on the Surface Ozone Forecast in the Greater Athens Area, Greece, *Advances in  
769 Meteorology*, 2012, 894714, <https://doi.org/10.1155/2012/894714>, 2012.

770 Mukherjee, A., Yadav, D. S., Agrawal, S. B., and Agrawal, M.: Ozone a persistent challenge to food security in India:  
771 Current status and policy implications, *Current Opinion in Environmental Science & Health*, 19, 100220,  
772 <https://doi.org/10.1016/j.coesh.2020.10.008>, 2021.

773 Pleijel, H., Danielsson, H., and Broberg, M. C.: Benefits of the Phytotoxic Ozone Dose (POD) index in dose-response  
774 functions for wheat yield loss, *Atmospheric Environment*, 268, 118797,  
775 <https://doi.org/10.1016/j.atmosenv.2021.118797>, 2022.

776 Sacks, W. J., Deryng, D., Foley, J. A., and Ramankutty, N.: Crop planting dates: an analysis of global patterns, *Global  
777 Ecology and Biogeography*, 19, 607-620, <https://doi.org/10.1111/j.1466-8238.2010.00551.x>, 2010.

778 Sahu, S. K., Liu, S., Liu, S., Ding, D., and Xing, J.: Ozone pollution in China: Background and transboundary contributions  
779 to ozone concentration & related health effects across the country, *Sci Total Environ*, 761, 144131,  
780 <https://doi.org/10.1016/j.scitotenv.2020.144131>, 2021.

781 Shang, Y., Sun, Z., Cao, J., Wang, X., Zhong, L., Bi, X., Li, H., Liu, W., Zhu, T., and Huang, W.: Systematic review of  
782 Chinese studies of short-term exposure to air pollution and daily mortality, *Environment International*, 54, 100-111,



783 <https://doi.org/10.1016/j.envint.2013.01.010>, 2013.

784 Sindelarova, K., Granier, C., Bouarar, I., Guenther, A., Tilmes, S., Stavrakou, T., Müller, J. F., Kuhn, U., Stefani, P., and  
785 Knorr, W.: Global data set of biogenic VOC emissions calculated by the MEGAN model over the last 30 years, *Atmos.*  
786 *Chem. Phys.*, 14, 9317-9341, <https://doi.org/10.5194/acp-14-9317-2014>, 2014.

787 Tai, A. P. K., Mickley, L. J., Heald, C. L., and Wu, S.: Effect of CO<sub>2</sub> inhibition on biogenic isoprene emission: Implications  
788 for air quality under 2000 to 2050 changes in climate, vegetation, and land use, *Geophysical Research Letters*, 40,  
789 3479-3483, <https://doi.org/10.1002/grl.50650>, 2013.

790 Tai, A. P. K., Sadiq, M., Pang, J. Y. S., Yung, D. H. Y., and Feng, Z.: Impacts of Surface Ozone Pollution on Global Crop  
791 Yields: Comparing Different Ozone Exposure Metrics and Incorporating Co-effects of CO<sub>2</sub>, *Frontiers in Sustainable*  
792 *Food Systems*, 5, <https://doi.org/10.3389/fsufs.2021.534616>, 2021.

793 Travis, K. R., Jacob, D. J., Fisher, J. A., Kim, P. S., Marais, E. A., Zhu, L., Yu, K., Miller, C. C., Yantosca, R. M., Sulprizio,  
794 M. P., Thompson, A. M., Wennberg, P. O., Crounse, J. D., St. Clair, J. M., Cohen, R. C., Laughner, J. L., Dibb, J. E.,  
795 Hall, S. R., Ullmann, K., Wolfe, G. M., Pollack, I. B., Peischl, J., Neuman, J. A., and Zhou, X.: Why do models  
796 overestimate surface ozone in the Southeast United States?, *Atmos. Chem. Phys.*, 16, 13561-13577,  
797 <https://doi.org/10.5194/acp-16-13561-2016>, 2016.

798 van der Werf, G. R., Randerson, J. T., Giglio, L., van Leeuwen, T. T., Chen, Y., Rogers, B. M., Mu, M., van Marle, M. J.  
799 E., Morton, D. C., Collatz, G. J., Yokelson, R. J., and Kasibhatla, P. S.: Global fire emissions estimates during 1997–  
800 2016, *Earth Syst. Sci. Data*, 9, 697-720, <https://doi.org/10.5194/essd-9-697-2017>, 2017.

801 Van Dingenen, R., Dentener, F. J., Raes, F., Krol, M. C., Emberson, L., and Cofala, J.: The global impact of ozone on  
802 agricultural crop yields under current and future air quality legislation, *Atmospheric Environment*, 43, 604-618,  
803 <https://doi.org/10.1016/j.atmosenv.2008.10.033>, 2009.

804 Wang, H., Lyu, X., Guo, H., Wang, Y., Zou, S., Ling, Z., Wang, X., Jiang, F., Zeren, Y., Pan, W., Huang, X., and Shen, J.:  
805 Ozone pollution around a coastal region of South China Sea: interaction between marine and continental air, *Atmos.*  
806 *Chem. Phys.*, 18, 4277-4295, <https://doi.org/10.5194/acp-18-4277-2018>, 2018a.

807 Wang, H., Lu, X., Jacob, D. J., Cooper, O. R., Chang, K. L., Li, K., Gao, M., Liu, Y., Sheng, B., Wu, K., Wu, T., Zhang, J.,  
808 Sauvage, B., Nédélec, P., Blot, R., and Fan, S.: Global tropospheric ozone trends, attributions, and radiative impacts  
809 in 1995–2017: an integrated analysis using aircraft (IAGOS) observations, ozonesonde, and multi-decadal chemical  
810 model simulations, *Atmos. Chem. Phys.*, 22, 13753-13782, <https://doi.org/10.5194/acp-22-13753-2022>, 2022a.

811 Wang, L., Tai, A. P. K., Tam, C.-Y., Sadiq, M., Wang, P., and Cheung, K. K. W.: Impacts of future land use and land cover  
812 change on mid-21st-century surface ozone air quality: distinguishing between the biogeophysical and biogeochemical  
813 effects, *Atmos. Chem. Phys.*, 20, 11349-11369, <https://doi.org/10.5194/acp-20-11349-2020>, 2020.

814 Wang, L., Wang, S., Zhou, Y., Liu, W., Hou, Y., Zhu, J., and Wang, F.: Mapping population density in China between 1990  
815 and 2010 using remote sensing, *Remote Sensing of Environment*, 210, 269-281,  
816 <https://doi.org/10.1016/j.rse.2018.03.007>, 2018b.

817 Wang, T., Xue, L., Feng, Z., Dai, J., Zhang, Y., and Tan, Y.: Ground-level ozone pollution in China: a synthesis of recent  
818 findings on influencing factors and impacts, *Environmental Research Letters*, 17, 063003,  
819 <https://doi.org/10.1088/1748-9326/ac69fe>, 2022b.

820 Wang, X., Gong, G., Li, N., and Qiu, S.: Detection Analysis of Epileptic EEG Using a Novel Random Forest Model  
821 Combined With Grid Search Optimization, *Frontiers in Human Neuroscience*, 13,  
822 <https://doi.org/10.3389/fnhum.2019.00052>, 2019.

823 Wang, Y., Zhang, Y., Hao, J., and Luo, M.: Seasonal and spatial variability of surface ozone over China: contributions from  
824 background and domestic pollution, *Atmos. Chem. Phys.*, 11, 3511-3525, <https://doi.org/10.5194/acp-11-3511-2011>,  
825 2011.

826 Wang, Y., Wild, O., Ashworth, K., Chen, X., Wu, Q., Qi, Y., and Wang, Z.: Reductions in crop yields across China from

827 elevated ozone, *Environmental Pollution*, 292, 118218, <https://doi.org/10.1016/j.envpol.2021.118218>, 2022c.

828 Wei, J., Li, Z., Li, K., Dickerson, R. R., Pinker, R. T., Wang, J., Liu, X., Sun, L., Xue, W., and Cribb, M.: Full-coverage  
829 mapping and spatiotemporal variations of ground-level ozone (O<sub>3</sub>) pollution from 2013 to 2020 across China, *Remote  
830 Sensing of Environment*, 270, 112775, <https://doi.org/10.1016/j.rse.2021.112775>, 2022.

831 Wesely, M. L.: Parameterization of surface resistances to gaseous dry deposition in regional-scale numerical models,  
832 *Atmospheric Environment* (1967), 23, 1293-1304, [https://doi.org/10.1016/0004-6981\(89\)90153-4](https://doi.org/10.1016/0004-6981(89)90153-4), 1989.

833 Wild, O. and Prather, M. J.: Global tropospheric ozone modeling: Quantifying errors due to grid resolution, *Journal of  
834 Geophysical Research: Atmospheres*, 111, <https://doi.org/10.1029/2005JD006605>, 2006.

835 Xiao, Q., Chang, H. H., Geng, G., and Liu, Y.: An Ensemble Machine-Learning Model To Predict Historical PM<sub>2.5</sub>  
836 Concentrations in China from Satellite Data, *Environmental Science & Technology*, 52, 13260-13269,  
837 <https://doi.org/10.1021/acs.est.8b02917>, 2018.

838 Yang, L., Luo, H., Yuan, Z., Zheng, J., Huang, Z., Li, C., Lin, X., Louie, P. K. K., Chen, D., and Bian, Y.: Quantitative  
839 impacts of meteorology and precursor emission changes on the long-term trend of ambient ozone over the Pearl River  
840 Delta, China, and implications for ozone control strategy, *Atmos. Chem. Phys.*, 19, 12901-12916,  
841 <https://doi.org/10.5194/acp-19-12901-2019>, 2019.

842 Yin, H., Pizzol, M., and Xu, L.: External costs of PM<sub>2.5</sub> pollution in Beijing, China: Uncertainty analysis of multiple health  
843 impacts and costs, *Environmental Pollution*, 226, 356-369, <https://doi.org/10.1016/j.envpol.2017.02.029>, 2017a.

844 Yin, P., Chen, R., Wang, L., Meng, X., Liu, C., Niu, Y., Lin, Z., Liu, Y., Liu, J., Qi, J., You, J., Zhou, M., and Kan, H.:  
845 Ambient Ozone Pollution and Daily Mortality: A Nationwide Study in 272 Chinese Cities, *Environ Health Perspect*,  
846 125, 117006, <https://doi.org/10.1289/EHP1849>, 2017b.

847 Yin, Z. and Ma, X.: Meteorological conditions contributed to changes in dominant patterns of summer ozone pollution in  
848 Eastern China, *Environmental Research Letters*, 15, <https://doi.org/10.1088/1748-9326/abc915>, 2020.

849 Zhan, Y., Luo, Y., Deng, X., Chen, H., Grieneisen, M. L., Shen, X., Zhu, L., and Zhang, M.: Spatiotemporal prediction of  
850 continuous daily PM<sub>2.5</sub> concentrations across China using a spatially explicit machine learning algorithm,  
851 *Atmospheric Environment*, 155, 129-139, <https://doi.org/10.1016/j.atmosenv.2017.02.023>, 2017.

852 Zhang, W., Feng, Z., Wang, X., Liu, X., and Hu, E.: Quantification of ozone exposure- and stomatal uptake-yield response  
853 relationships for soybean in Northeast China, *Science of The Total Environment*, 599-600, 710-720,  
854 <https://doi.org/10.1016/j.scitotenv.2017.04.231>, 2017.

855 Zhang, X., Osei, F., Stein, A., Cheng, C., and Maji, K. J.: Temporal and spatial evolution of short-term exposure to ozone  
856 pollution: Its health impacts in China based on a meta-analysis, *Journal of Cleaner Production*, 373, 133938,  
857 <https://doi.org/10.1016/j.jclepro.2022.133938>, 2022a.

858 Zhang, X., Yan, B., Zhou, Y., Osei, F., Li, Y., Zhao, H., Cheng, C., and Stein, A.: Short-term health impacts related to ozone  
859 in China before and after implementation of policy measures: A systematic review and meta-analysis, *Science of The  
860 Total Environment*, 847, 157588, <https://doi.org/10.1016/j.scitotenv.2022.157588>, 2022b.

861 Zhang, Y., Wang, Y., Gao, M., Ma, Q., Zhao, J., Zhang, R., Wang, Q., and Huang, L.: A Predictive Data Feature Exploration-  
862 Based Air Quality Prediction Approach, *IEEE Access*, 7, 30732-30743,  
863 <https://doi.org/10.1109/ACCESS.2019.2897754>, 2019.

864 Zhang, Z., Yao, M., Wu, W., Zhao, X., and Zhang, J.: Spatiotemporal assessment of health burden and economic losses  
865 attributable to short-term exposure to ground-level ozone during 2015-2018 in China, *BMC Public Health*, 21, 1069,  
866 <https://doi.org/10.1186/s12889-021-10751-7>, 2021.

867 Zhao, Z. and Wang, Y.: Influence of the West Pacific subtropical high on surface ozone daily variability in summertime  
868 over eastern China, *Atmospheric Environment*, 170, 197-204, <https://doi.org/10.1016/j.atmosenv.2017.09.024>, 2017.

869 Zhou, D., Ding, A., Mao, H., Fu, C., Wang, T., Chan, L. Y., Ding, K., Zhang, Y., Liu, J., Lu, A., and Hao, N.: Impacts of  
870 the East Asian monsoon on lower tropospheric ozone over coastal South China, *Environmental Research Letters*, 8,

871  
872

044011, <https://doi.org/10.1088/1748-9326/8/4/044011>, 2013.